Conduction at domain walls
in insulating $Pb(Zr_{0.2}Ti_{0.8})O_3$ thin films

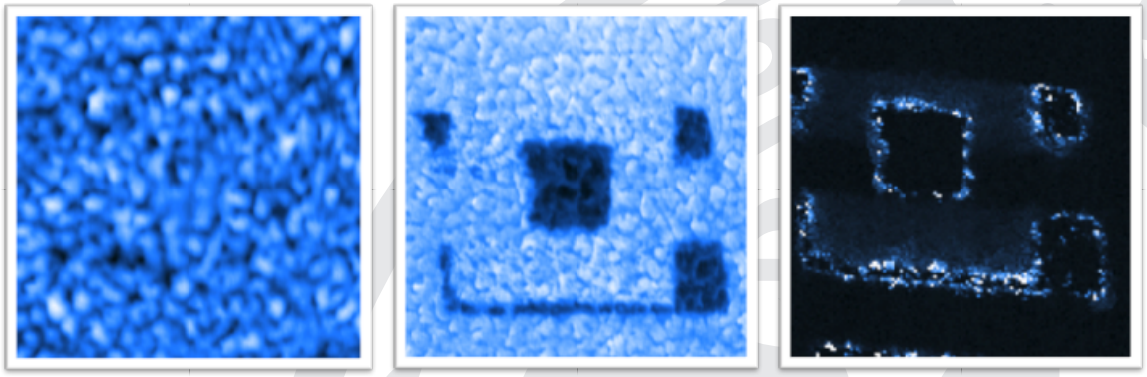

Thesis

Presented to the Faculty of Sciences of the University of Geneva
for a degree of Master in Physics

By

IAROSLAV GAPONENKO
Département de la Physique de la Matière Condensée, Université de Genève

SUPERVISOR:

Prof. Patrycja Paruch

I am among those who think that science has great beauty.
A scientist in his laboratory is not only a technician:
he is also a child placed before natural phenomena
which impress him like a fairy tale.
Marie Curie, 1867-1934

Contents

1 Acknowledgements

This work has been done in the context of a Master in Physics, under the supervision of Prof. Patrycja Paruch. All of the measurements were taken and analyzed jointly with Jill Guyonnet, with whom we went through the gates of hell and returned with a beautiful publication.

I wholeheartedly thank Prof. Patrycja Paruch for welcoming me in her laboratory from my first summer internship up to the present day, and for introducing me to the wonderful realm of nanoscale materials science. I also thank her for being my advisor, and thoroughly correcting numerous iterations of the chapters in this thesis, and for being flexible with my greatest nemesis - deadlines.

I am grateful to Dr. Pavlo Zubko and Dr. Igor Stolichnov, who have kindly agreed to be part of the jury for the thesis defense.

I am infinitely indebted to Jill Guyonnet for the time we spent working on this project, squashing program bugs and making pretty plots.

I would especially like to thank Sebastien Muller and Marco Lopes for their technical support and expertise. Without them, the lab would have turned to fire and brimstone a long time ago.

My recognition also goes to all of my colleagues from the groups of Prof. Paruch and Prof. Triscone. I am grateful to Dr. Pavlo Zubko for countless helpful discussions, his encyclopedic knowledge and always good advice, and I thank Dr. Stefano Gariglio for his samples and expertise on lead zirconate titanate.

I also thank Dr. Romain Stomp from SPECS-Zurich for taking time to explain the inner workings of the Nanonis controller.

I would like to warmly thank my family and friends, with a special shout to Mila Lomarda, who has supported me all along despite her strong aversion to physics.

Finally, I bow to the patient reader, who will not flinch at the shifty grammar or laugh at a dubious vocabulary.

2
Introduction

As technological pressure for ever smaller and power-efficient devices continues, materials science seeks to find alternative pathways to multi-functionality at the nanoscale. Interfaces are an example of such systems with reduced dimensionality, and have been shown to possess interesting physics through new or reduced symmetries and strong electron correlation effects, leading to potentially novel phenomena. One type of interface in oxide materials are ferroic domain walls, which occur naturally as a way to optimize the depolarization energy costs, and are intrinsically nanoscale. They allow for multiple possible orientations of spontaneous electric polarization, magnetization or strain, and have been shown to possess properties differing from their parent materials [7]. Recent work has focused on the multiferroic $BiFeO_3$ [6], where electrical conduction has been reported in 180°, 109° [45] and 71° [13] domain walls.

Here, we demonstrate domain wall conduction in a simple ferroelectric tetragonal perovskite material, $Pb(Zr_{0.2}Ti_{0.8})O_3$. We show that the phenomenon occurs separately from polarization switching and is highly stable in time. Moreover, we establish a highly asymmetric and nonlinear current-voltage characteristic relationship, with evidence of thermal activation at temperatures above 150K. Our analysis of the current-voltage relationship in the framework of different possible conduction mechanisms suggests that both the transfer of charge from the metallic atomic force microscope tip into the ferroelectric film past the interfacial Schottky barrier, and the subsequent motion of charge through the domain wall but not the bulk of the material inside the domain need to be considered. An important role is clearly played by the structure of the domain walls themselves, where charged segments stabilized by screening charges from defects or mobile carriers can increase the conductivity. To discriminate between the two likeliest mechanisms - Richardson-Schottky-Simmons (interface limited but addressing the bulk via the mobility term) and Poole-Frenkel (bulk limited, but potentially assisted by tunneling or emission at the interface) - further studies in terms of temperature and thickness dependence are under way.

This work begins with an introduction to the theoretical aspects of ferroelectric materials, followed by an overview of conduction mechanisms previously reported therein. Domain walls and their electronic properties are discussed, with a focus on the recent results of $BiFeO_3$ domain wall conduction and their relevance to the present work. The theoretical section is followed by a presentation of the $Pb(Zr_{0.2}Ti_{0.8})O_3$ samples used in the course of the investigation on domain wall conduction, whose crystalline quality is demonstrated by x-ray characterization. We then describe the atomic force microscopy techniques used to create, image and characterize

the domain wall structure.

Results on domain wall conduction are then presented, beginning with the observation of domain wall conduction with conductive atomic force microscopy. The time-dependent characteristics of the observed conduction are characterized with position-and-hold measurements, and time-dependent current-voltage characteristics are extracted first from alternating conductive atomic force microscopy and piezoresponse force microscopy measurements, and second from grid spectroscopy measurements. The dynamic nature of the conduction is then discussed, with hysteretic measurements on domain walls revealing multiple regimes. Finally, the conduction mechanisms presented in the theoretical section are used to analyze the observed current-voltage characteristics, yielding the plausible domain wall conduction mechanisms. This work ends with a take on the microscopic origin of the conductivity and a conclusion with an outlook on the further experiments.

There is a theory which states that if ever anybody discovers exactly what the Universe is for and why it is here, it will instantly disappear and be replaced by something even more bizarre and inexplicable. There is another theory which states that this has already happened.

D. Adams

3 Theoretical background

By analogy with ferromagnets, which can have a stable net magnetization reversible by the application of a magnetic field, ferroelectrics are materials possessing a net spontaneous electric polarization, the orientation of which can be switched by the application of an electric field. Ferroelectrics also have the property of being pyroelectric and piezoelectric, responding to temperature variations and mechanical stress, respectively, with the appearance of an electric dipole moment. Since the first ferroelectric material, Rochelle salt, was discovered by Valasek in 1920, hundreds more have been reported to be ferroelectric. Ferroelectric materials are now present in virtually every aspect of daily life, mostly in the form of sensors or memories. Examples of their use include ferroelectric RAM chips, fuel injectors, thermal vision cameras, and sonars.

3.1 Ferroelectric materials

In order for a material to be ferroelectric, there have to be two or more stable, switchable, polarization states present. Moreover, the switchable polarization has to remain stable once the electric field is removed. In order to characterize a ferroelectric crystal, the polarization is measured as a function of applied voltage, usually by sweeping the applied voltage across a set voltage range at a specific frequency and temperature. A typical polarization versus voltage relationship, showing the ferroelectric hysteresis loop of a lead zirconate titanate thin film is shown in Fig. 3.1. When the applied voltage reaches a critical value, called the coercive voltage $Vc+$ or $Vc-$, switching from one polarization state to another occurs. The polarization then saturates at a value depending on the material, $Ps+$ or $Ps-$, and stabilizes at its remanent value $Pr+$ or $Pr-$ when the voltage is brought to zero. The ferroelectric switching is accompanied by switching currents at the coercive voltage. These are transient and will decay with time, after all of the ferroelectric has switched. The ideal ferroelectric loop is symmetric, with polarizations in both states being equal. In reality, it depends on the sample and its boundary conditions.

3.1.1 Piezoelectric properties

As mentioned above, piezoelectricity is also present in all ferroelectrics. This means that once stress is applied to the material, polarization will arise (direct piezoelectric effect). The same effect is also present in the other direction, with the application of an electric field giving rise to material strain-induced deformation (converse piezoelectric effect). The set of equations

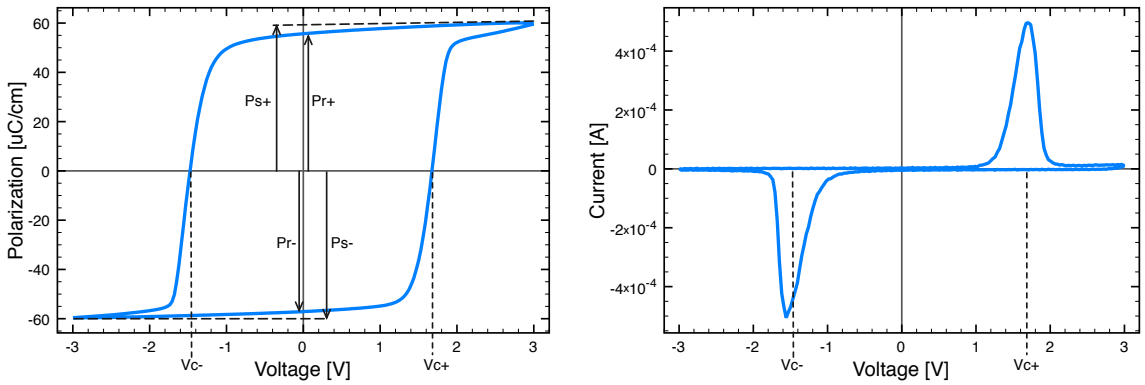

Figure 3.1: A lead zirconate titanate thin film hysteresis loop, courtesy of Dr. Stefano Gariglio. The polarization versus voltage curve on the left shows a ferroelectric hysteresis loop with two stable states with opposite remanent polarization $Pr+$ and $Pr-$. The switching between them occurs as the voltage applied crosses a threshold voltage $Vc+$ or $Vc-$ respectively. The polarization saturates at $Ps+$ or $Ps-$ and decreases to its remanent value once the voltage is removed. The right curve shows the corresponding current measured through the sample during the voltage sweep. In equilibrium, a ferroelectric is insulating and current does not flow. When switching occurs, it is accompanied by strong currents due to polarization reversal.

governing the direct and converse piezoelectric effects can be expressed as:

$$P_i = b_{ijk}\sigma_{jk}$$

$$\epsilon_{ij} = E_k b_{kij}$$

with P the polarization vector, b the piezoelectric tensor, σ the stress tensor, ϵ the strain tensor, E the electric field vector. Moreover, conservation of energy leads to the fact that the piezoelectric tensor is the same for the piezoelectric effect as well as the converse piezoelectric effect both effects. This tensor is material-specific and depends strongly on the symmetries of the crystal, thus restricting the possible polarization vector directions. A tetragonal uniaxial ferroelectric having a single out of plane polarization axis with two possible states $S1$ and $S2$, would have a tensor such as the one shown below dictated by symmetry considerations:

$$b_{ijk}^{S1} = \begin{bmatrix} 0 & 0 & 0 & 0 & 2b_{113} & 0 \\ 0 & 0 & 0 & 2b_{113} & 0 & 0 \\ b_{311} & b_{311} & b_{333} & 0 & 0 & 0 \end{bmatrix}$$

$$b_{ijk}^{S2} = \begin{bmatrix} 0 & 0 & 0 & 0 & -2b_{113} & 0 \\ 0 & 0 & 0 & -2b_{113} & 0 & 0 \\ -b_{311} & -b_{311} & -b_{333} & 0 & 0 & 0 \end{bmatrix}$$

3.1.2 Thermodynamics

A successful phenomenological theory describing the ferroelectric phase transition has been developed by Devonshire, using the Ginzburg-Landau formalism initially applied to magnetic systems. This theory is based purely on thermodynamic considerations. The free energy, U, is expanded around the transition in terms of the polarization P:

$$U = \frac{\alpha}{2}P^2 + \frac{\gamma}{4}P^4 + \frac{\delta}{6}P^6 - EP$$

with the definition $\alpha = \beta(T - T_c)$, T_c the transition temperature, $\beta > 0$, $\delta > 0$ and γ depending on the order of the phase transition (negative for first and positive for second order). Plotting

this expression in Fig. 3.2 with different temperatures shows the appearance of a double well in the free energy with two different and opposite polarization values as the temperature is lowered below the critical temperature T_c, indicating a broken symmetry accompanying the ferroelectric phase transition. The system will take on one of the energy equivalent polarization ground states in order to reduce its free energy, explaining the ferroelectric phase transition. The addition of a voltage to the free energy expression allows to understand the ferroelectric switching qualitatively. The voltage will tilt the potential, and once it reaches a critical value, the energy barrier preventing the polarization from reorienting will be overcome and the free energy will thus be lowered. In the case where the voltage is zero, the barrier is too high to be overcome, and the polarization is stable.

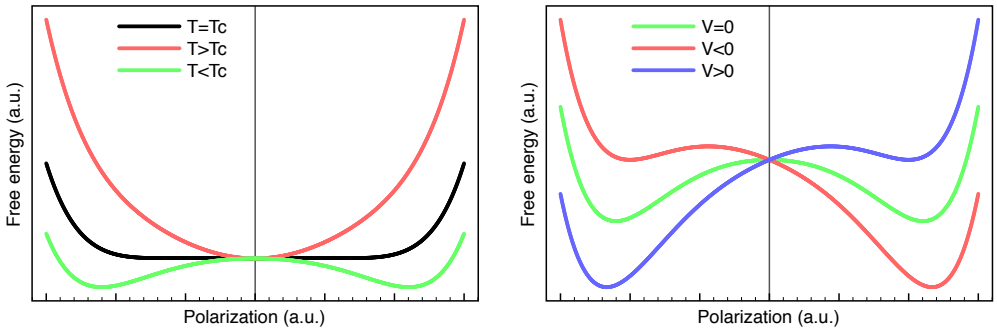

Figure 3.2: The free energy versus the polarization is plotted for different values of the temperature at zero voltage (left) and for different values of voltage below the critical temperature (right). Once the temperature lowers below the ferroelectric transition temperature, the symmetry is broken and the ferroelectric has two energy-equivalent polarization states. The application of a voltage tilts the potential profile, allowing for switching by overcoming the barrier between the two states.

3.1.3 Physical mechanism

Although the thermodynamic GLD theory does provide a good description of the macroscopic physics and allows the mean field properties of ferroelectric materials to be predicted, it does not explain microscopic phenomena such as the formation of the dipole moment. For the purpose of illustration, we will concentrate on the family of ferroelectric perovskites to which belongs the material under investigation in this research. The perovskite structure, named after the eponymous $CaTiO_3$, is composed of three types of atoms with a chemical formula ABO_3, with A a monovalent or divalent metal such as calcium, lead, bismuth or strontium, and B a tetravalent or pentavalent metal such as zirconium, titanium or iron. The structure is cubic with the corners populated with A atoms and the B atom in the center, surrounded by an oxygen octahedron. One such perovskite ferroelectric is $PbTiO_3$ (PTO). It is shown in its paraelectric state, above the ferroelectric transition temperature, in Fig. 3.3. Below the transition temperature, it is a uniaxial tetragonal ferroelectric, and although the mechanism behind the formation of the dipole moment is complex, involving the covalent bonds between the constituents of the unit cell giving rise to a Born effective charge, it can be considered as almost purely displacive: the opposite movement of the positive and negative charge centers creates the electric dipole giving rise to the two energy-equivalent polarization states P_{up} and P_{down}.

Regions of different uniform polarization within a ferroelectric are called domains. These domains are stable, and depending on the boundary conditions and on the material can either span the whole of the material or form periodic domains of different sizes. The preference a

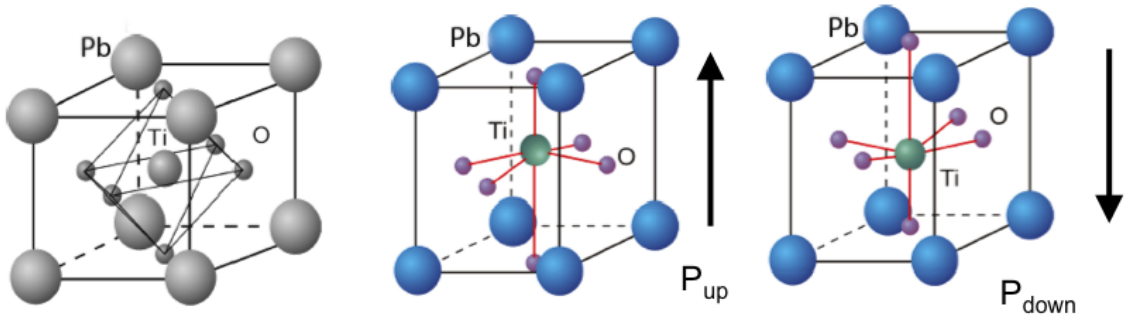

Figure 3.3: $PbTiO_3$ is a textbook perovskite ferroelectric, with a cubic paraelectric ground state at high temperatures. As the symmetry-breaking structural phase transition occurs, a spontaneous polarization appears due to the microscopic dipolar moment originating from the titanium and oxygen displacements. Two stable configurations are possible, P_{up} and P_{down}. The paraelectric cubic state unit cell dimension is 3.957Å. For the tetragonal state at room temperature, the 3.893Å and 4.138Å have been measured.

material will have for either of these possibilities will depend on the screening of the polarization at the surface with electrodes, impurities or charge accumulation [7]. However, one can estimate the domain configuration by calculating the energy of the possible strucures. This was done by Kittel for the case of a ferromagnetic thin film [28], and the result is shown in Fig. 3.4. Three configurations are considered: flux closure, polydomain out of plane and monodomain

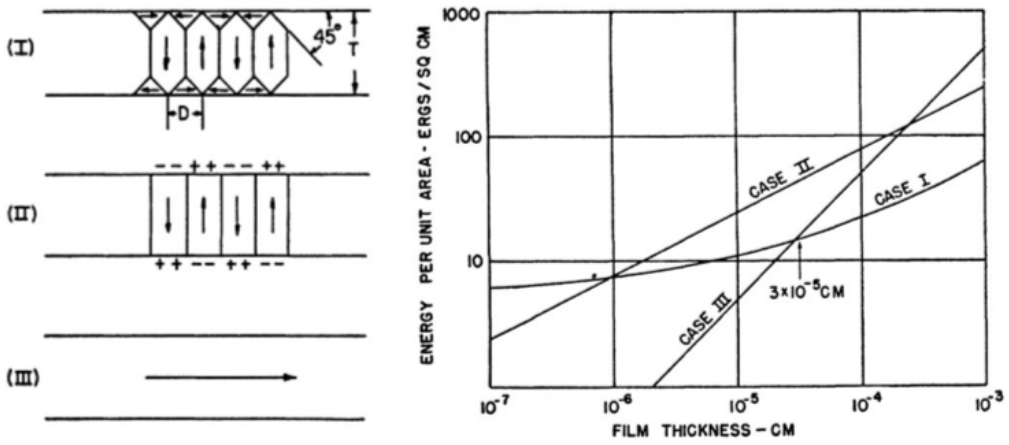

Figure 3.4: The energy of several domain configurations is examined by Kittel for ferromagnetic materials as a function of material thickness. It can be seen that for very thin films, the best configuration is monodomain, followed by closure domains at intermediate thickness and periodic out-of-plane domains in thick films.

in plane. This calculation shows that for a ferromagnetic thin film the most energetically favourable domain configuration is monodomain in plane followed by a transition to closure domains at intermediate thickness, and eventually a periodic out of plane domain strucure for thick films. In ferromagnetic materials, where the magnetization is related to the ordering of microscopic spins, anod no monopoles exist, the type of domain structure is defined by the energy balance between the energy cost of divergent or unclosed field lines originating from the magnetic structure, and the energy cost of the domain wall. For a periodic, out-of-plane domain structure, the balance between these two terms will determine the period width, obeying the Landau-Lifshitz-Kittel scaling:

$$w = \sqrt{\frac{\sigma}{U} d}$$

with w the period of the domain structure, d the thickness of the film, U the volume energy density of the domain and σ the energy density per unit area of the domain wall. This scaling is also applicable to ferroelectrics in the case where the polarization is unscreened, or only weakly screened. We note from the data of domain period versus thickness presented in Fig. 3.5 that the domain periodicity in such structures is much higher for ferroelectric films, meaning smaller domains. This relates to a generally Ising-like domain with a much thinner domain wall structure, as opposed to Bloch or Neel type walls in ferromagnets, associated with the polarization being related to the actual crystal structure and symmetry rather than the spin orientation which generally has much more freedom to rotate. However, an additional key factor in fer-

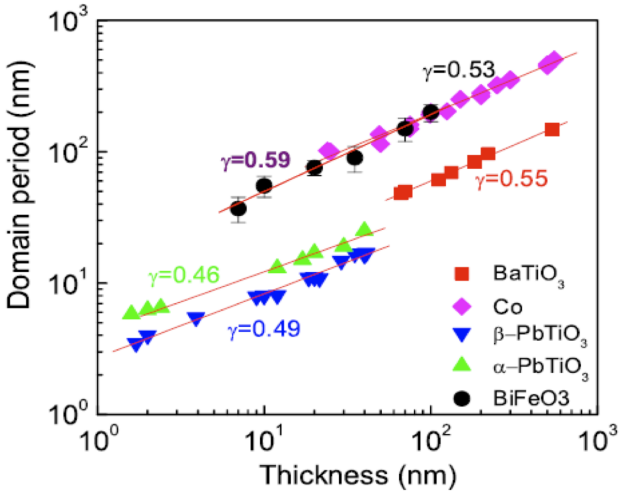

Figure 3.5: Kittel's square root law for domain wall width in function of film thickness for ferroic materials. The relationship is linear for each of the materials, and the slope is very similar. From [5].

roelectrics is the presence of charges which can screen the polarization provided for example by adjacent metallic electrodes, surface charge accumulation under specific environmental conditions, or the presence of internal mobile charges due to defects such as oxygen vacancies. Thus, electrical boundary conditions as well as film thickness and domain wall energy density determine the final configuration which can be either monodomain or polydomain [30, 15, 47].

Thanks to the effects of polarization screening, stable artificial domains of various sizes can also be created by means of electrical poling. In this experiment, an atomic force microscope tip has been used as an electrode in order to write domains for analysis on a monodomain as-grown film.

3.1.4 Domain walls

When more than one domain is present in a ferroelectric sample, the boundary separating the domains is called a domain wall. This wall has a finite thickness over which the polarization changes progressively. The study of domain walls started with ferromagnetic materials and has shown that several types of domain wall exist, some of which are illustrated in Fig. 3.6c-e. It was found that their width in ferromagnets is of the order of hundreds of nanometers, in contrast with ferroelectrics, where domain walls are of the order of a nanometer. due to the possibility for ferroelectric polarization to change its magnitude. [7] The change of polarization at the domain wall has been extensively studied theoretically and experimentally. It was found for lead titanate that with the constraint of no in-plane polarization (purely Ising walls), the domain wall thickness at the ground state was of the order of unit cells [38, 33]. More recent

calculations by Lee *et al* with a possibility of free rotation of the polarization vector show that in lead titanate the domain walls have a mixed Ising-Neel type such as the one shown in Fig. 3.6f [29]. The Ising character is dominant, but there is a very small in-plane component of the polarization appearing just at the domain wall, as shown in Fig. 3.6b. The domain wall thickness also agrees with the previous calculations. Thanks to recent technological advances, it

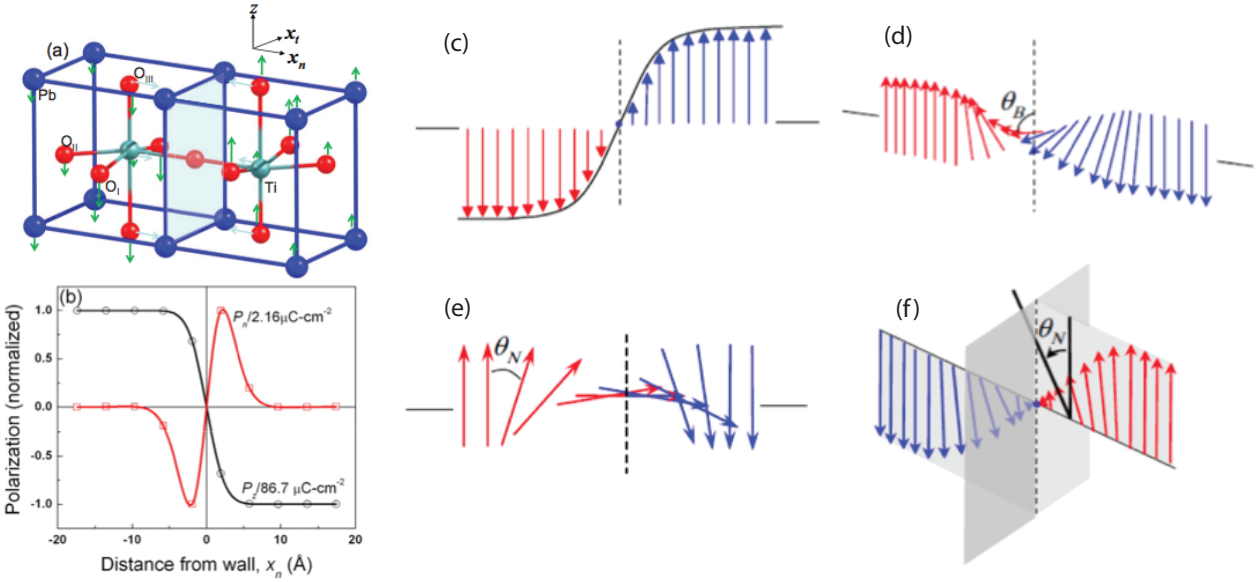

Figure 3.6: a) Atomic displacements across the domain wall in PTO modeled by DFT. b) Normalized polarization cell by cell shows that there is an in-plane component to the polarization (red) at the out of plane polarization switching (black). c) Ising type domain wall, with a change of polarization amplitude without any rotation. d) Bloch type domain wall, with a rotation θ_B of the polarization along the domain wall, with a constant polarization vector magnitude. e) Neel type domain wall with a θ_N rotation across the domain wall, with a constant polarization vector magnitude. f) Mixed Ising-Neel domain wall, where the polarization vector decreases and rotates at the same time. From [29].

is also possible to experimentally look at 180° domain walls at the atomic scale with techniques such as high resolution aberration corrected transmission electron microscopy or holographic electron microscopy. A recent work by Jia *et al* illustrates a 180° domain wall in a lead zirconate titanate perovskite ferroelectric, shown in Fig. 3.7 [27]. The images reveal several interesting features. First, the domain wall does present an Ising-type magnitude decrease of the polarization vector in good agreement with the DFT models. Second, the wall is not straight, but shows the presence of steps a few unit cells wide along its length. At such steps, the microscopic dipole moment are anti-aligned, an energetically highly unfavorable configuration which could, by itself, not remain stable. However, the presence of charged defects at the domain wall could screen the polarization discontinuity and stabilize the steps. Finally, near the interface with the strontium ruthenate, which is only 2.5 unit cells thick and thus expected to provide only very weak screening, a polarization rotation appears in order to provide a closure domain minimizing the energy required to maintain this domain configuration.

Thus, domain walls are interfaces that can be seen as topological defects, showing changes in symmetry and strain at the nanoscale. Moreover, they are intrinsically linked with defects: either defects segregate at domain walls or domain walls get pinned to defects which lower their energy potential [23]. To add to this complex behavior, coupling between different ferroic orders can occur in more complex materials such as $BiFeO_3$, a ferroelectric, ferroelastic, antiferromagnetic multiferroic, in which magnetism is predicted to arise at 109° domain walls [7]. To conclude, the intrinsically nanoscale nature of the domain walls in ferroelectrics can potentially lead to the discovery of novel functionalities therein.

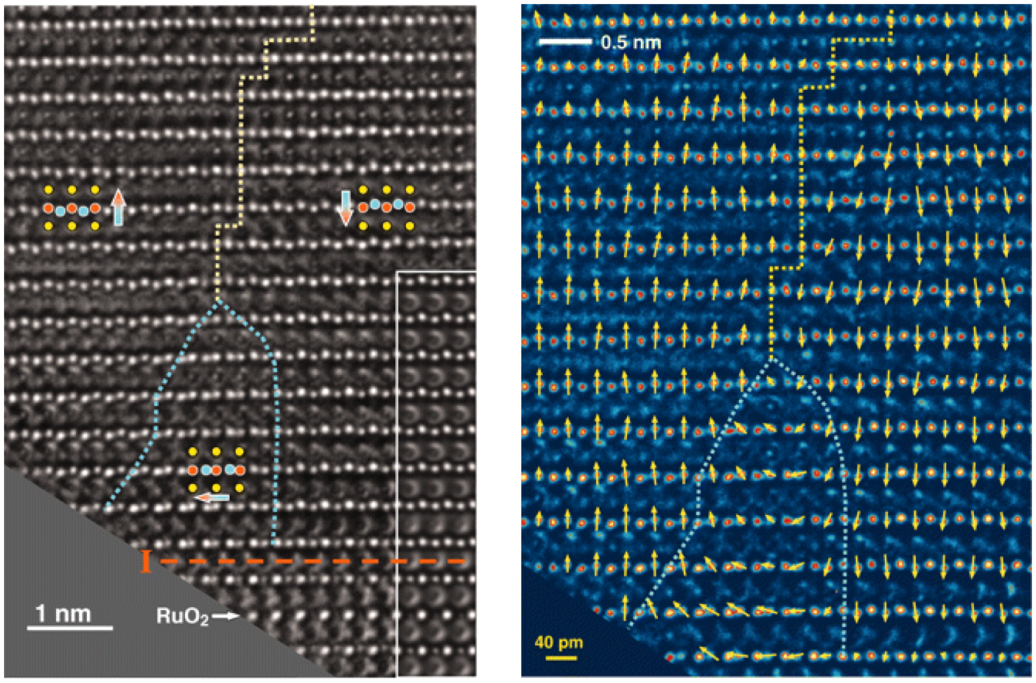

Figure 3.7: HR-TEM image of a 180° domain wall in a lead-zirconate-titanate thin film grown on strontium titanate with a strontium ruthenate electrode. The right image is colorized in order to show the atomic displacement vectors. The domain wall is shown to have an Ising-like behavior with a non-trivial spatial configuration, possibly stabilized by defects.

3.2 Conduction mechanisms in solids

In this section we will discuss several conduction mechanisms which occur in semiconducting and insulating materials. Ferroelectrics are essentially wide band gap insulators with some charge mobility due to defects, and the following mechanisms have all been investigated or proposed for different temperatures or boundary conditions in ferroelectric materials.

The usual way to describe electrical conduction mechanisms makes use of the current versus voltage relationships. In metals, conduction occurs by the movement of charge carriers and scattering from scattering centers, giving rise to Ohm's law, a linear relationship between the current and the voltage with the conductivity σ as the proportionality constant:

$$I = \sigma V$$

In semiconductors, the mechanisms are more complex, and can, for instance, not involve a drift motion of charge through the solid, but rather hopping, diffusion or electron-hole pair formation and recombination. Thus, the relationship between the current and voltage for a semiconductor is usually non-linear and can present a complex dependence on temperature and boundary conditions. A measurement of the current-voltage (I-V) characteristic curve allows us to extract the relationship between the current and the electric field to determine which microscopic conduction mechanism dominates the I-V behavior in the sample.

3.2.1 Bulk or interface?

The conduction mechanisms for semiconductors described below can be separated into two broad categories: bulk limited and interface limited. This separation can be understood in terms of the largest obstacle to overcome for the charge carriers in order to flow through the solid. For interface-limited mechanisms, the biggest barrier is at the interface between the bulk of the material and its boundaries, be it vacuum or electrodes. For the bulk-limited case, the

interfaces do not matter and the conduction is governed by the bulk of the material. As an example, let us consider a basic measurement setup, shown in Fig. 3.8. A semiconductor is connected to a voltage source and current meter by the means of two metallic contacts. Determining the conduction mechanism in this case is a nontrivial task, because there are three barriers to overcome for charge carrier flow: the first metal-semiconductor interface, the bulk of the semiconductor and finally the last semiconductor-metal interface. In the ideal case, one mechanism will be dominant, as it happens with textbook semiconductors, but the worst case scenario with two different electrode materials with their own work functions involves three competing mechanisms, especially when one introduces the polarization or chemical interactions. Thus, finding out the conductivity of such a system is not a trivial problem.

In the following we will detail the following mechanisms:

- Bulk:
    1. Space charge limited (SCL)
    2. Poole-Frenkel hopping (PF)
- Interface:
    1. Schottky thermionic emission (SE)
    2. Richardson-Schottky-Simmons (RSS)
    3. Fowler-Nordheim tunneling (FN)

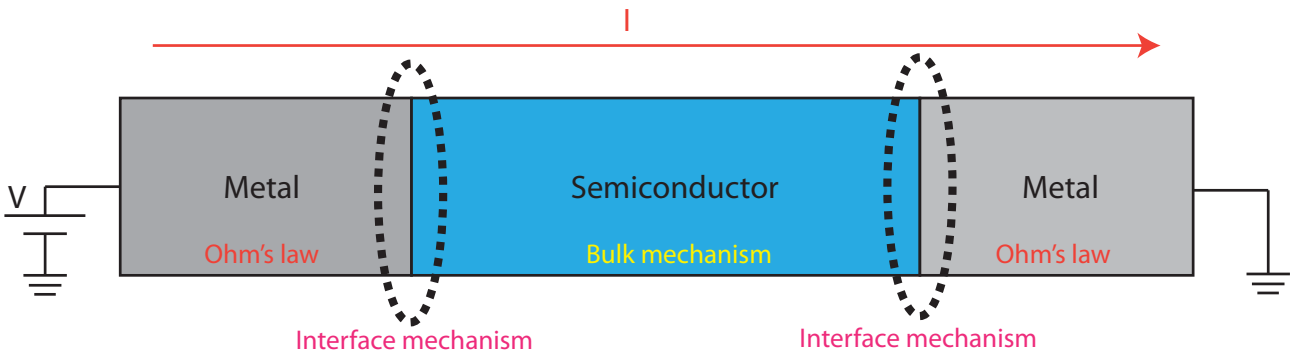

Figure 3.8: Typical experimental setup for simple transport measurements: a voltage V is applied and a current I will flow between two electrodes forming a junction with the probed semiconductor. The bulk of the semiconductor as well as the interfaces will alter the transport characteristics of the system.

3.2.2 Space charge limited conduction

For SCL, let us consider the case of ideal ohmic contacts on a semiconductor. Once a voltage is applied to the system, charge will flow freely through the metal and enter the semiconductor, providing a high carrier density near the metal-semiconductor interface. This will in turn diffuse the carriers into the bulk due to the self-generated electric fields. Moreover, this mechanism is highly dependent on defects in the material since they provide trap states enhancing the carrier diffusion. The general form of the current is therefore proportional to a power of the applied voltage:

$$I \propto V^n$$

with n an exponent depending on the exact physics of the material. A value of $n = 2$ is expected in the case of discrete traps, whereas values of $n > 2$ indicate that the trap states are distributed

in the middle of the gap. In the latter case, a specific thermal dependence is expected: for an exponential trap distribution, $n - 1 = \frac{T_1}{T}$ with T_1 the characteristic temperature; and for a Gaussian trap distribution, $(n-1)^2 = 1 + \frac{2\pi\sigma_t^2}{16k_b^2T^2}$, with σ_t the standard deviation. Finally, for the case of discrete traps distributed in the sample, one expects to have a quadratic dependence on the voltage [52]:

$$I = \frac{9}{8}\theta_f \varepsilon \varepsilon_0 \mu \frac{V^2}{d^3}$$

with μ the carrier mobility, ε the dielectric constant of the medium under consideration, ε_0 the vacuum dielectric constant, θ_f the fraction of non-trapped charge carriers, d the sample thickness, and V the applied voltage.

In order to fit the current voltage curves we will use the linearization of the space charge limited conduction mechanism:

$$\log(I) \propto \log V$$

This will yield linear regions conforming to this mechanism, and whose slope will yield the exponent n.

3.2.3 Poole-Frenkel hopping

Poole-Frenkel hopping also assumes that the contact between the metal and the semiconductor is ohmic, as the charge first needs to get into the semiconductor unhampered by any potential barriers. A physical picture of Poole-Frenkel hopping can be drawn by looking at what happens

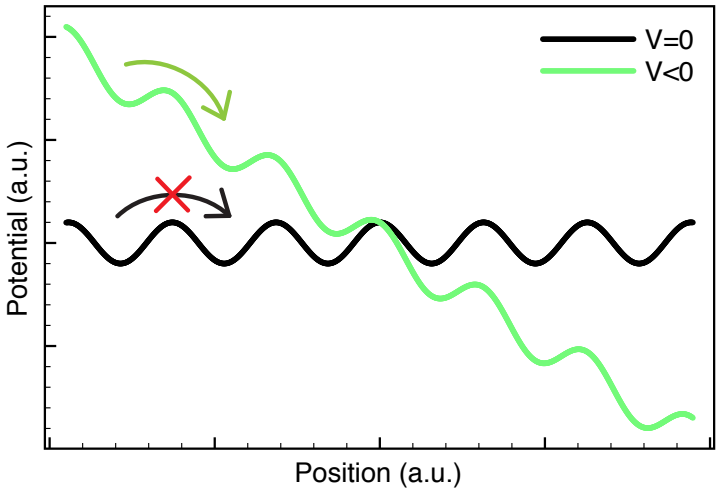

Figure 3.9: Potential in a semiconductor with evenly distributed trap states. The application of an electric field tilts this washboard potential from its equilibrium position where the charge carriers do not have enough energy to hop from one state to another (black) to a state where charge carriers can hop from one trap to another (green), along the slope created by the electric field. This is the conduction mechanism of Poole-Frenkel hopping.

to evenly spread trap states when one applies an electric field to the material. Trap states being essentially potential wells, the global potential throughout the sample resembles a washboard, such as the one shown in the black curve of Fig. 3.9. Once the electric field is applied, the washboard tilts (green line), and the charge carriers can escape their trap state into the next one by overcoming a small barrier to reach a lower potential, located at a different trap state.

This mechanism is thus thermally activated as can be seen from the functional dependence:

$$I = \sigma_0 E \exp\left(-\frac{E_t}{k_B T}\right) \exp\left(\beta_{PF}\sqrt{E}\right)$$

$$\beta_{PF} = 2\beta = 2\frac{e}{k_B T}\left(\frac{e}{4\pi\varepsilon\varepsilon_0}\right)^{1/2}$$

with E the electric field, E_t the trap energy, k_B the Boltzmann constant, T the temperature, σ_0 the sample dependent zero field conductivity, ε the dielectric constant of the medium under consideration and ε_0 the vacuum dielectric constant [52].

For fitting current voltage curves, we will use the linearization:

$$\log(I/E) \propto \sqrt{E}$$

This gives a linear dependence in the region where the current behaves like a Poole-Frenkel hopping mechanism.

3.2.4 Schottky thermionic emission

At the interface between a metal and a semiconductor one usually has a potential barrier, referred to as a Schottky barrier. This barrier can be overcome by the application of a bias, and the needed energy can be lowered even further by the thermal excitation of charge carriers. A schematic representation of this is shown in Fig. 3.10, with a metal far, close and in contact with a semiconductor. The formula expressing the current voltage characteristic of this conduction

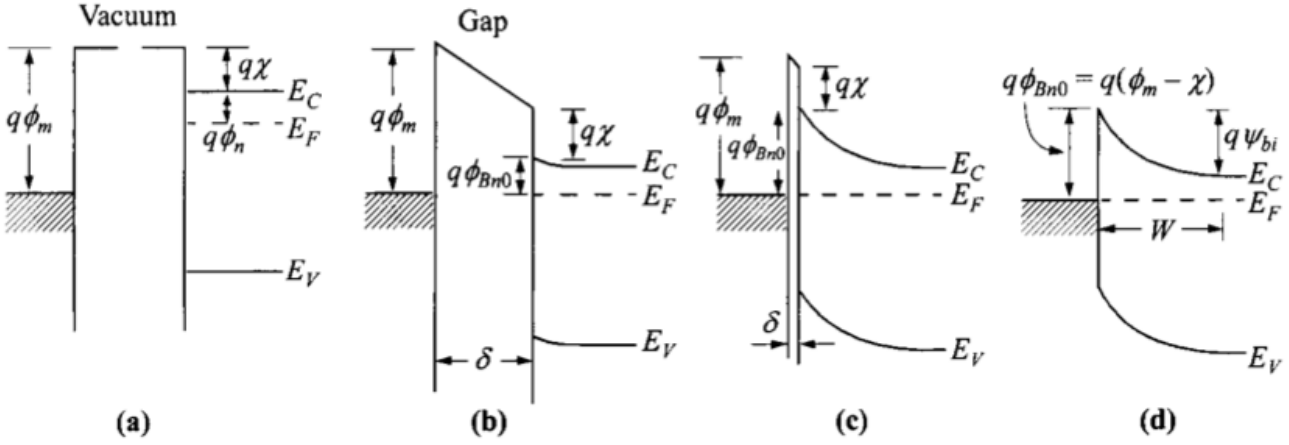

Figure 3.10: A metal-semiconductor contact has different properties depending on the material characteristics. If the workfunction of the metal is lower than the chemical potential in the semiconductor, as the contact is made electrons will flow from the semiconductor conduction band into the metal. The accumulation of charge will have the effect of deforming the band structure, giving rise to a Schottky barrier. Here, the metal and semiconductor are (a) completely insulated from one another by a very large distance in vacuum, (b) brought close together with a gap δ, (c) when $\delta \to 0$ and finally (d) in contact. From [48]

mechanism with the explicit thermal dependence is:

$$I = A^* T^2 \exp\left(-\frac{q\phi_{B0}}{k_B T}\right) \exp\left(\beta\sqrt{E_m}\right)$$

$$\beta = \frac{e}{k_B T}\left(\frac{e}{4\pi\varepsilon\varepsilon_0}\right)^{1/2}$$

with $A^* = 4\pi e m^* k_B^2/h^3$ the Richardson constant with $m*$ the effective mass, k_B the Boltzmann and h the Planck constants, ϕ_{B0} the barrier height, q the carrier charge, e the electron charge and E_m the field at the potential maximum, giving the Schottky barrier decrease [52]. For instance, in the case of a uniform field, or full depletion, one can assume $E_m = V/d$. For the case of partial depletion, also referred to as abrupt junction, there will be an in-built bias in the material:

$$E_m = \sqrt{\frac{2qN_D}{\varepsilon_{dc}\varepsilon_0}\left(V + V_{bi} - \frac{k_B T}{q}\right)}$$

with N_D the dopant concentration, V_{bi} the built-in bias and $k_B T/q$ a term originating from the free carriers in the depletion layer.

A linearization of the Schottky thermionic emission mechanism is done with either the full ($E \propto V$) or partial depletion ($E \propto \sqrt{V + V_{bi}}$) expressions:

$$\log(I/T^2) \propto \sqrt{E}$$

and gives linear regions of data from which physical constants such as the barrier height or the dielectric constant can be extracted.

3.2.5 Richardson-Schottky-Simmons

A special case of the Schottky interface-mediated conduction arises when the mean free path is very short compared to the dimension of the material (low mobility case). This scenario can be expected in ferroelectric materials. In this case, the Richardson-Schottky-Simmons formulation can be applied:

$$I = 2e\left(\frac{2\pi m k_B T}{h^2}\right)^{3/2} \mu E \exp\left(-\frac{\phi}{k_B T}\right) \exp\left(\beta\sqrt{E}\right)$$

$$\beta = \frac{e}{k_B T}\left(\frac{e}{4\pi\varepsilon\varepsilon_0}\right)^{1/2}$$

with m the effective mass, k_B the Boltzmann and h the Planck constantsd, e the electron charge, ϕ the barrier height, μ the bulk mobility and E the electric field [46]. Due to the bulk mobility appearing in this interface-limited mechanism, RSS is peculiar because although it is an interface limited mechanism, it addresses the mobility of the bulk.

The linearization for fitting current versus voltage data is given by:

$$log(I/E) \propto \sqrt{E}$$

and allows to compute physical quantities like the barrier height and the dielectric constant.

3.2.6 Fowler-Nordheim tunneling

Fowler-Nordheim tunneling is another interface limited mechanism. However, instead of overcoming the barrier at the interface by classical means, the charge carriers tunnel through from the electrode Fermi level into the conduction band of the semiconductor, as shown in Fig. 3.11. [16, 40]

$$I = \frac{q^3 m}{8\pi h m^* \phi_b} E^2 \exp\left(-\frac{8\pi\sqrt{2m^*}}{3qh}\frac{1}{E}\right)$$

with E the electric field, q the carrier charge, m and m^* the free and effective electron masses, h the Planck constant and ϕ_b the barrier height.

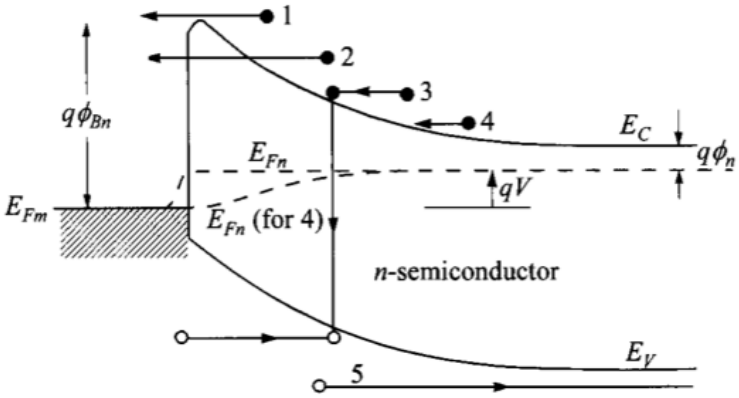

Figure 3.11: There are five mechanisms for current to arise through a Shottky barrier: 1) thermionic emission 2) tunneling 3) recombination 4) diffusion of electrons and 5) diffusion of holes. For the Fowler-Nordheim mechanism, the width of the barrier is small enough for the charge carriers to tunnel through. From [48]

It is possible to linearize the above equation as shown previously:

$$\log(I/E^2) \propto -1/E$$

The plots of the current data reveal linear regions which can be attributed to Fowler-Nordheim tunneling. with E the applied field. Moreover, this mechanism does not have a temperature dependence, and thus any thermal gradient cannot be attributed to FN.

3.2.7 Conduction in ferroelectrics

Although for many purposes ferroelectric materials can be seen as ideal insulators, this is far from being the case in reality. There are three major sources of current in all real samples:

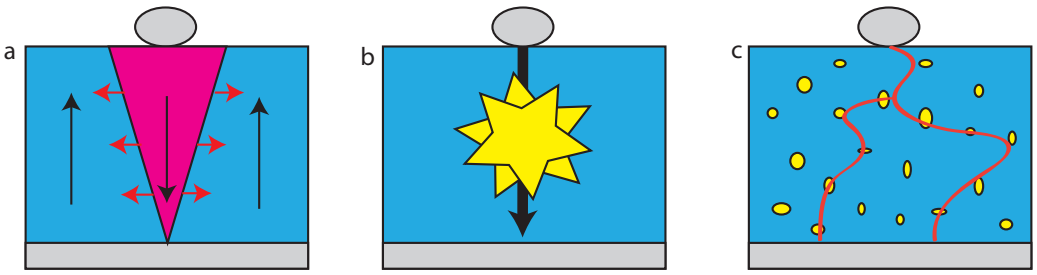

Figure 3.12: A schematic image for sources of current in real ferroelectrics. (a) Polarization switching, (b) Electric breakdown, occuring at very high fields. (c) Leakage, due to the presence of defects.

- **Switching (Fig. 3.12a):** The switching of the polarization from one orientation to another is accompanied by transient currents called switching currents. A ferroelectric switching current can come from two sources: domain nucleation and domain wall displacement. The domain nucleation current is short in duration, of the order of a millisecond, and high in intensity, of the order of nanoamperes for thin films up to milliamperes for single crystals and can be described as a pulse. Domain wall motion is much less intense but longer in duration, decaying exponentially as the domain wall moves away from the electric field center.

- **Breakdown (Fig. 3.12b):** A ferroelectric, or any wide band gap insulator, will be susceptible to an electrical breakdown when submitted to a sufficiently high field. This occurs when the charge carriers are accelerated sufficiently by the field to produce other charge carriers when colliding with the lattice atoms. This process is highly destructive and usually alters the ferroelectric in an irreversible way, for example by creating permanent conducting channels.

- **Leakage (Fig. 3.12c):** Most ferroelectrics, and especially thin films, are not perfect insulators, for instance due to defects. Indeed, they display leakage, which allows for current to flow through the material at higher fields. This mechanism is different from breakdown, as it is not an irreversible threshold process, but a gradual increase of current with voltage. Ferroelectric fatigue, after repeated cycling of switching the polarization can also create leakage. This degrades the properties of the ferroelectric to the extreme where switching becomes impossible.

More recently, there has been a significant focus on thin film ferroelectrics, with a particular attention to their use for ferroelectric tunneling junctions. An example of this is shown in Fig. 3.13, with the nanometer-scale ferroelectric sandwiched by two metallic electrodes. The polarization as well as piezoelectric strain will change the current-voltage characteristics of the tunneling barrier, rendering it useful for practical applications. Another recent discovery, tun-

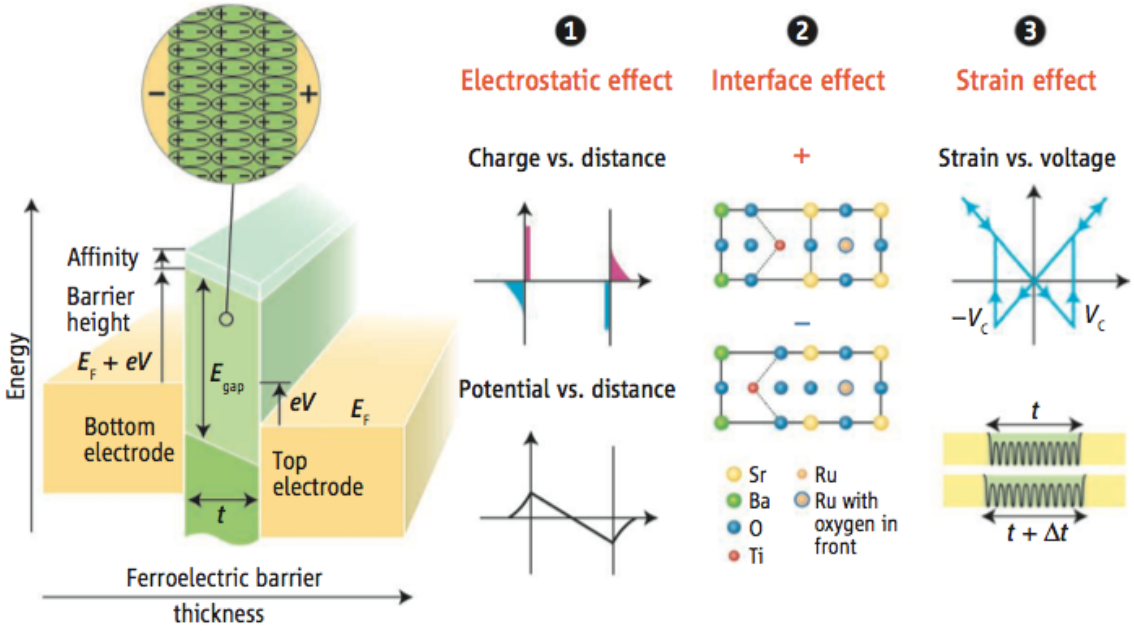

Figure 3.13: A schematic image for a ferroelectric tunnel junction. E_{gap} is the ferroelectric band gap, E_F is the Fermi energy of the electrodes, V is the applied voltage, V_c is the coercive voltage, t is the barrier thickness and Δt its variation. Two metallic electrodes are separated by a very thin ferroelectric film. Thus, the application of an electric field can switch the ferroelectric polarization orientation, and change the resistance of the junction (tunneling electroresistance). The responsible mechanisms are the change in electrostatic potential at the barrier, the change in tunneling transmission coefficient at the interfaces and the change in attenuation constant of the barrier. From [49]

neling electroresistance has been observed in ultrathin insulating $BaTiO_3$ [19, 21], $PbTiO_3$ [9] and $Pb(Zr_{0.2}Ti_{0.8})O_3$ [31]. The resistance was probed by means of conductive atomic force microscopy, and was found to differ by several orders of magnitude depending on the ferroelectric polarization orientation, paving the way to resistive ferroelectric memories with *ON* or *OFF* states.

A different pathway to conduction in generally insulating oxide materials is presented by topological defects, such as twin walls or domain walls in multiferroic and ferroelectric materials. This includes superconducting domain walls in Na-dopes WO_3 [2], insulating antiphase boundaries at domain walls in $YMnO_3$, or, more pertinent to this research, the discovery of domain wall conduction in multiferroic $BiFeO_3$. It has been shown that 109°, 180° as 71° domain walls conduct [45, 13]. This is illustrated in Fig. 3.14, where the current at fixed voltage and ferroelectric polarization are mapped by means of conductive atomic force microscopy and piezoresponse force microscopy respectively.

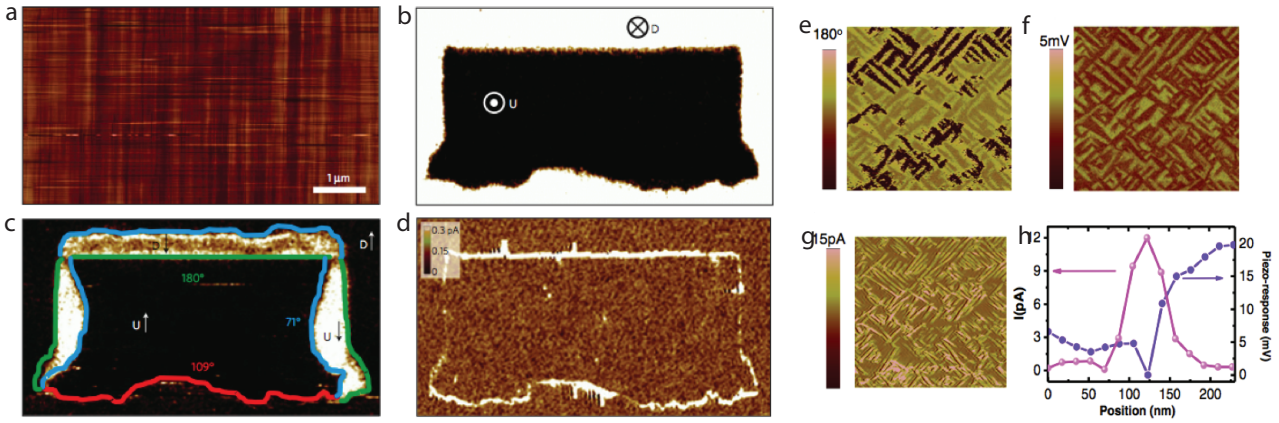

Figure 3.14: Domain wall conduction in $BiFeO_3$. The topography a) does not show any features, and the vertical b) and lateral c) piezoresponse force microscopy allow to determine the domain orientation of the artificially written structure to be determined. Current d) is shown to be located at 109° and 180° domain walls. A subsequent research on a BFO sample with as-grown 71° domains shows the lateral PFM phase e) and amplitude f), with a conductive AFM signal in g). The width of the domain wall and current signal are compared in h). From [45, 13]

One of the first explanations for this conduction, an intrinsic mechanism, involved the lowering of the band gap at the domain wall which was predicted by DFT calculations to be of 0.20eV, 0.10eV and 0.05eV for 180°, 109° and 71° domain walls respectively. The lack of observed current at the 71° domain walls was attributed to a too low bandgap lowering. However, later measurements of the effective bandgap by local scanning tunneling microscopy measurements [8] show that the local reduction in the bandgap of 71° and 109° domain walls is of the order of 0.20eV, and 0.50eV respectively. These measurements hint to the presence of localized states in the bandgap facilitating tunneling and conduction in the material.

Although no comparable calculations for the domain walls in PTO have been carried out, we can compare the DFT calculated band gap in the ferroelectric versus paraelectric phases. Depending on the method used, the band gap lowering at the cubic phase with respect to the tetragonal phase was calculated to be between 0.03eV and 0.6eV [3].

Another possibility, demonstrated by subsequent work on BFO domain walls is that the currents are not static (time-independent) but primarily dynamic, related to microscopic irreversible motion and change of the domain walls [32]. This was evidenced by a hysteresis window opening between the forward and backward curent-voltage curves acquired at the location of the domain wall, shown in Fig. 3.15 for different sweep voltage ranges. The explanation given for this phenomenon involves nanoscale displacements of the domain wall, which contribute to enhance the current signal, without saturating up to switching current levels.

Finally, there is the option that the domain wall conduction is related to the extrinsic charge

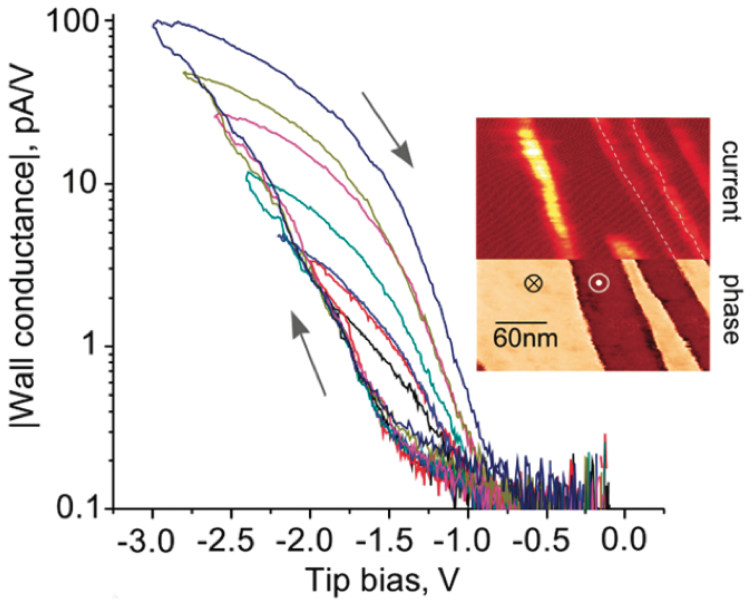

Figure 3.15: Dynamic nature of the domain wall conduction in BFO, shown for different values of sweep voltages. The hysteresis is omnipresent even for the lowest sweeps, hinting at a dynamic mechanism such as nanoscale domain wall motion. the inset shows the conductive-AFM and simultaneously acquired high resolution contact resonance PFM demonstrating that the current signal comes from the domain wall. From [32].

carriers, preferentially segregating at the domain walls, in particular to shield the polarization discontinuity leading to a potential step. This was also initially suggested by Seidel *et al* [45]. As demonstrated by the recent HRTEM work on domain walls in ferroelectrics [27, 26], even arguably much simpler 180° domain walls in tetragonal ferroelectrics such as PZT can show polarization discontinuities like steps, quadrant domains or head-to-head domain configurations. These discontinuities can only be stabilized by an accumulation of charged defects at the location of the wall. Ginzburg-Landau calculations performed for charged domain walls predict the existence of static conduction due to the presence of such charged defects [11]. The materials in which domain wall conduction has been shown are part of a large family of oxides, there has been a great deal of theoretical work on defects, and in particular on oxygen vacancies, showing their lower energy at a domain wall location [23, 39]. Experimental work has also explored the mobility of such defects and their segregation at domain walls, as well as their implications on polarization dynamics and conduction. [43, 42, 14]

Conduction in ferroelectric materials is thus not a trivial matter. Adding to this is the difficulty of separating the contribution of interfacial versus bulk mechanisms in macroscopic measurements. Therefore, although proper current-voltage characteristic curves are extracted by careful measurements, they may yield a combination of several of the mechanisms mentioned above. In the analysis of our data, we will be performing linearization of the acquired current values against these models to determine the dominating conduction mechanism in the system composed of our material and its front and back electrodes.

Why has not Man a microscopic eye?
For this plain reason, Man is not a Fly.
Say what the use, were finer optics giv'n,
T' inspect a mite, not comprehend the heav'n.

A. Pope, 1733

4 Materials and methods

4.1 Lead zirconate titanate

The material used in this research is a solid solution of antiferroelectric $PbZrO_3$ and ferroelectric $PbTi_3$ 20/80 in sputtered epitaxial thin film form. Its chemical formula can be written $Pb(Zr_{0.2}Ti_{0.8})O_3$. Its high temperature paraelectric state is a cubic perovskite (a=4.017Å) which undergoes a second order phase transition to the tetragonal ferroelectric structure (a≈3.96Å, c≈4.13Å for the sample in the present study) at 680°C[1]. The samples were grown on single crystal (001)-oriented $SrTiO_3$ (STO) substrates from *CrysTec* chosen for their high availability and compatibility with the unit cell a-axis of PZT (a=3.925Å). To allow the application of well defined fields for polarization switching, a back electrode of $SrRuO_3$ (SRO) of thickness 30-40nm was deposited first. The PZT film of thickness 60-70nm was then epitaxially grown on top of the SRO by means of off-axis RF magnetron sputtering by Dr. Stefano Gariglio [20].

As can be seen from Fig. 4.1, the x-ray scan of the (001) peaks along the (00l) reciprocal space direction shows very clear oscillations due to size effects on the side of the PZT peak indicating the high quality crystalline structure of the PZT. The PZT rocking curve full width half maximum of 0.228° can be compared to the STO substrate rocking curve FWHM of 0.087° in order to judge the film quality, which can also be seen in the reciprocal space map of the (103) reflections, shown in Fig. 4.2. The STO and SRO peaks are aligned vertically, whereas the PZT is slightly shifted. This indicates that although the SRO is constrained to the STO with the same a-axis, the PZT has relaxed close to its single-crystalline a-axis (3.95Å) and c-axis (4.14Å) unit cell parameters. Not only does the PZT grow epitaxially as shown before, but it also exhibits a very low surface roughness (0.2nm) and a good ferroelectric behaviour. This is shown in Fig. 4.3, where a sample topographic image and a microscopic phase-voltage loop are shown. Although switching is offset due to an inbuilt bias, the effect is not as pronounced as in Nb-doped STO substrate grown PZT, and did not affect our measurements adversely. A transmission electron microscopy image (Fig. 4.4) demonstrates very few a-axis inclusions throughout the PZT thin film, despite the presence of a multitude of defects in the substrate.

[1]This is a much higher value than the 460°C for the bulk PZT, due to the material being grown in epitaxial thin film form and thus subject to misfit strain.

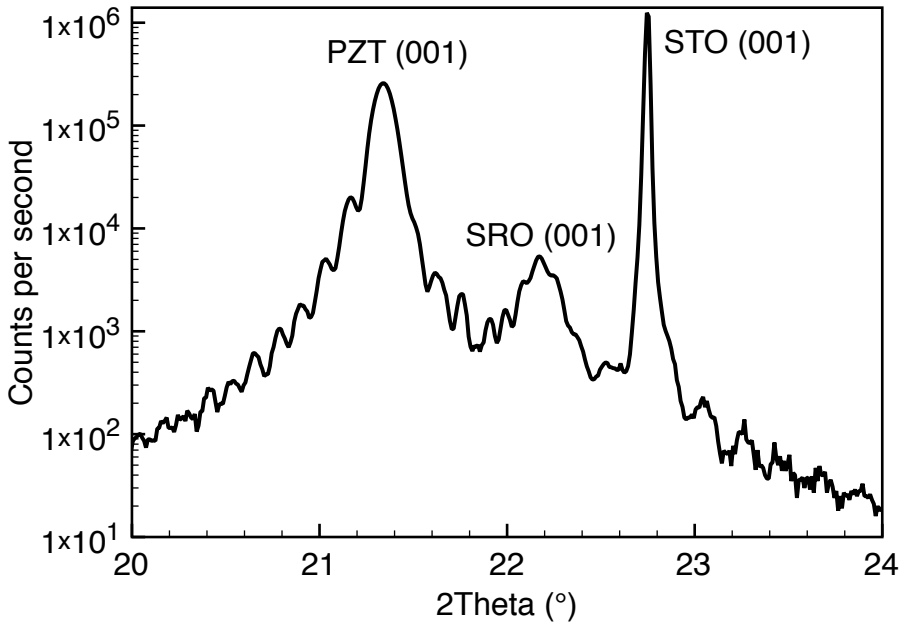

Figure 4.1: (001) scan of PZT/SRO/STO thin film, showing good crystallinity and size effect oscillations indicating a well-defined epitaxial layer.

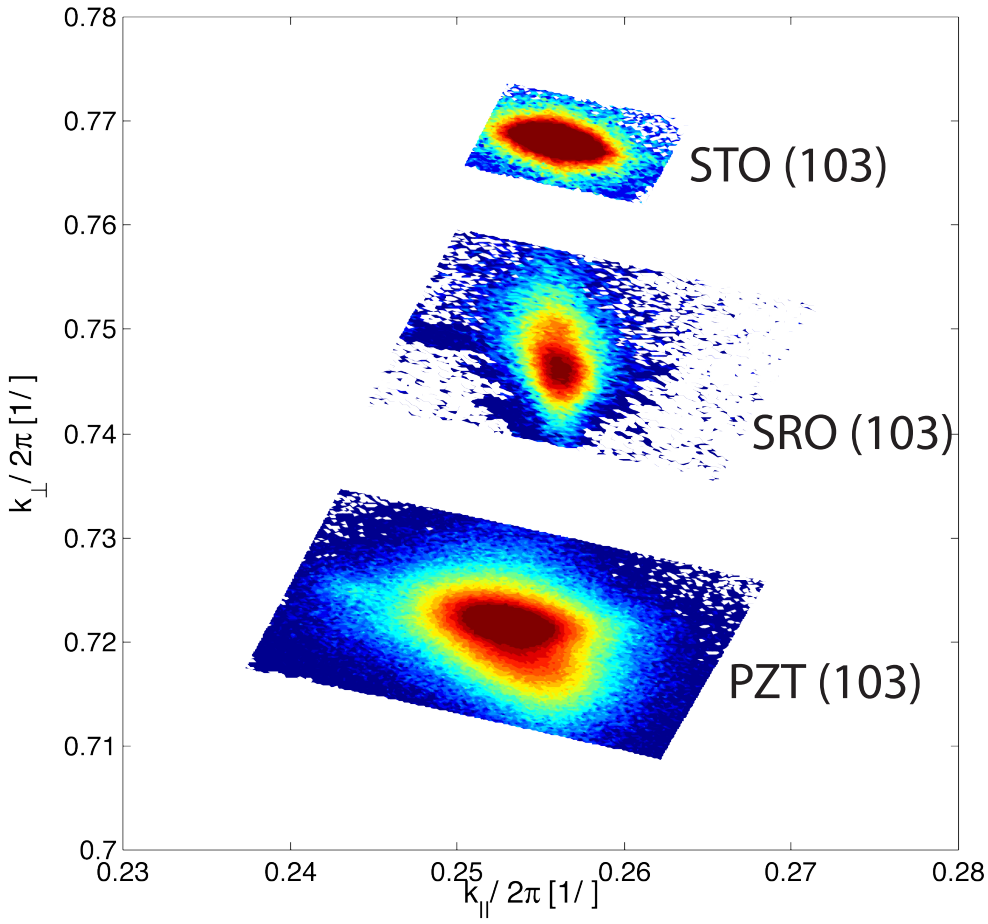

Figure 4.2: Reciprocal space map of the (103) reflections of PZT, SRO and STO in our thin films. The SRO is strained to the STO, but the PZT has relaxed to its bulk a-axis.

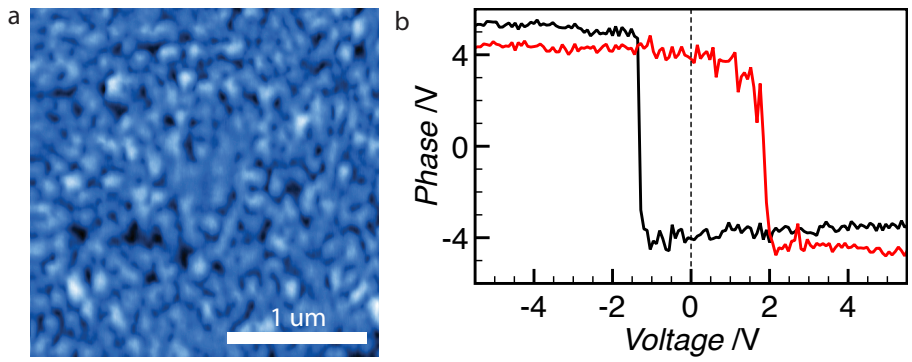

Figure 4.3: AFM topography (a) of the PZT sample used for this research, with a RMS roughness of 0.2nm. A piezoresponse force microscopy phase-voltage loop (b) demonstrates the ferroelectric character of the sample.

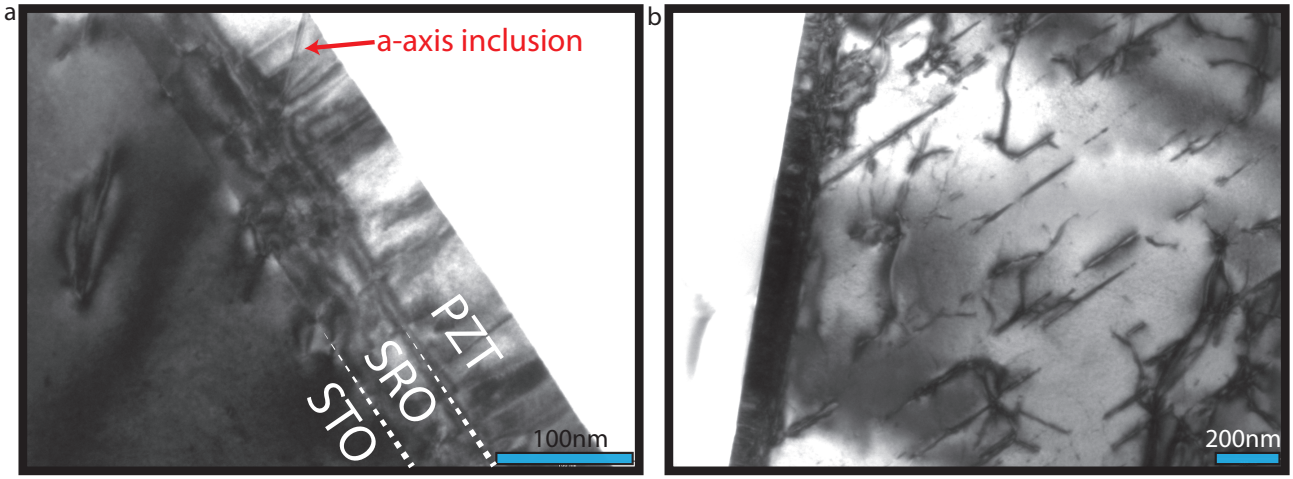

Figure 4.4: Transmission electron microscopy images of a PZT sample. (a) Small region showing the substrate STO, back electrode SRO and the PZT itself. A rare a-axis inclusion is pointed out by a red arrow. (b) A larger view shows the defects of the substrate. Images courtesy of Prof. Marin Alexe.

4.2 Atomic Force Microscopy

In order to locally characterization of the samples, we have performed measurements by means of an atomic force microscope (AFM). The AFM is a useful instrument for topographic and functional mapping of surfaces, and is used in such diverse fields as biology, chemistry and nanotechnology. Its concept was derived from the scanning tunneling microscope (STM) by the inventors of the latter [4]. The core of the design (Fig. 4.5) is a piezoelectric ceramic tube which acts as a nanopositioner. By exploiting the linear and reproducible voltage-displacement characteristic of piezoelectrics, the tube can be bent and extended in order to accommodate movements in all three directions. The typical accuracy is of the order of the nanometer in the X/Y directions, and of the order of an angstrom in the Z direction. Depending on the exact microscope model and design, the column is used to sweep the plane of either the sample or the pyramidal silicon tip (Fig. 4.6) and to adjust the distance between the two. In order to measure the interaction between the tip and the sample, a laser shines at a quadrant photo-sensitive detector (qPSD) by reflecting off the back of the tip cantilever.

With this simple design, the way measurements are performed is left up to the user and the capabilities of the controller's electronics. Several modes are consistently available across

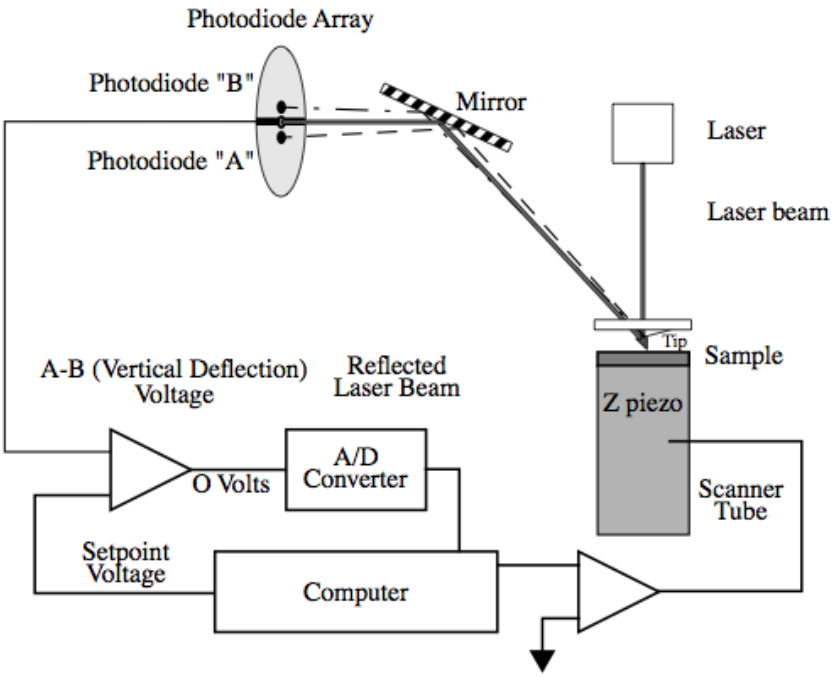

Figure 4.5: Schematics of a commercial AFM design with electronics configured for contact mode measurements. A laser bounces off the tip cantilever and its reflection's vertical deflection with respect to a quadrant photosensitive detector is used as a feedback parameter in order to control the Z extension of the piezo tube, allowing to image the sample topography. From [1]

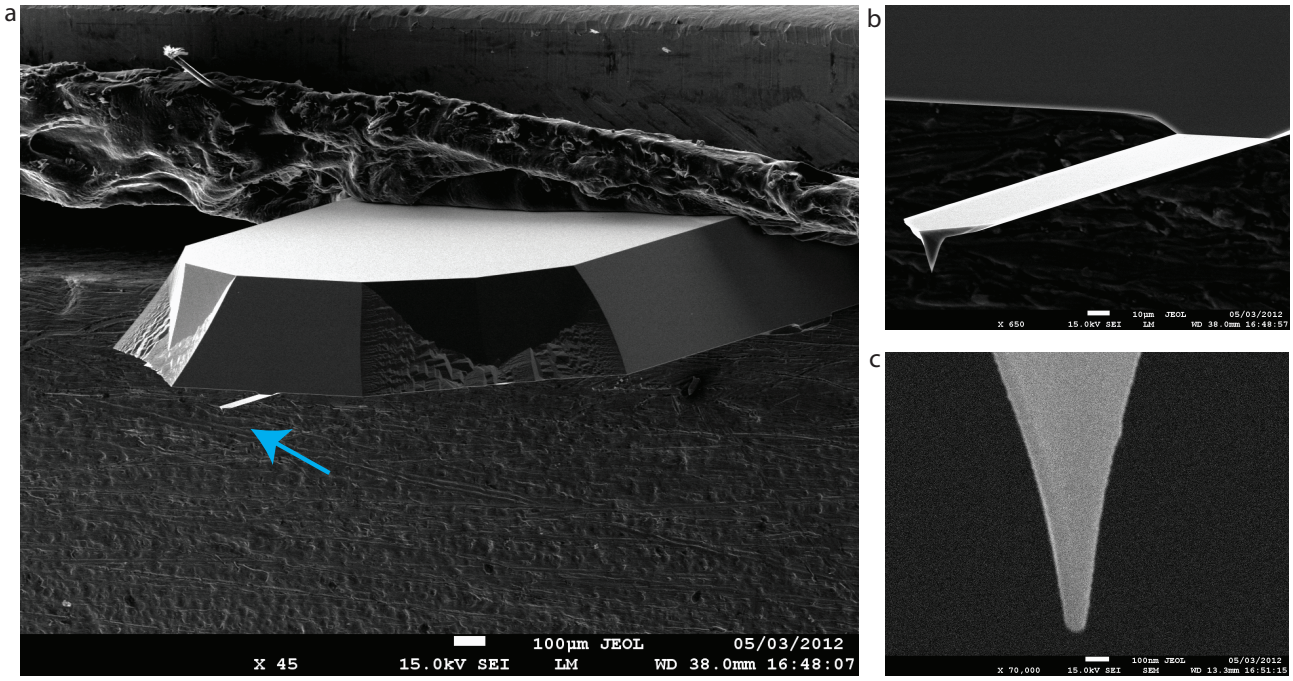

Figure 4.6: Scanning electron microscope images of a MESP AFM tip, with a nominal 20-50nm radius at pyramid apex. The cantilever beam geometry is tailored to optimize the tip resonance frequency and spring constant. (a) shows a 35X magnification, where the geometric shapes due to chemical etching are clearly visible, and the tip cantilever is indicated with the blue arrow. (b) is a 650X magnification on the cantilever, showing the pyramidal tip at the bottom and a flat back for laser reflection. (c) is an extreme 70000X magnification on the tip apex, showing that its radius of less than 50nm is consistent with the manufacturer's specifications.

the different commercial brands: contact mode, tapping mode, piezoresponse force microscopy and conductive AFM mode. The two latter ones were especially important for this research and are derived from (and used in conjunction with) contact mode AFM, so they will be mentioned under their respective headings. In order to measure the topography in contact mode, the controller contains a feedback loop responsible for continuously reading the vertical deflection from the qPSD and adjusting the Z position of the column as to keep the laser deflection constant. The extension of the column in the Z direction then gives the topographic information. For tapping mode, the tip is mechanically excited by a dither piezo slightly below its free resonance frequency. A lock-in amplifier then reads the qPSD vertical deflection in order to extract the amplitude and the phase of the oscillation. As the tip is brought in contact with the surface, the oscillation of the tip will be dampened. The feedback loop then adjusts the column extension in order to keep the dampening constant, thus giving a topographic image. Moreover, the response phase gives the information as to the composition of the sample since it depends strongly on the interaction between the tip and the sample.

For the purpose of this research we have done measurements in vacuum with a commercial AFM. The instrument is an Omicron VT Beam Deflection AFM/STM, allowing measurements from 800K down to 35K at the sample, with a scan range of 10μm x 10μm. The controller electronics have been changed from the original Omicron SCALA electronics to a Nanonis RC4, in order to provide more flexibility and better resolution. The system vacuum is typically of the order of $5 \circ 10^{-10}$mbar and loading of tips and samples is performed by means of a load lock thus minimizing the possibility of contamination. The sample is usually grounded but a direct access through the feedthrough connectors would allow it to be electrically biased if needed. Moreover, it is possible to attach a cryogenically cooled copper braid to the sample with the help of a clamping block. In this way, liquid nitrogen or liquid helium can be used to cool the sample down to 35K with the help of a liquid flow cryostat. This was used for the low temperature measurements presented later. The tip allows for an electrical contact and is used to pole ferroelectric domains by applying a DC voltage, to read the piezoresponse signal with an AC voltage or, in conjunction with a preamplifier, to measure a current. The tips used in this experiment were Bruker Probes MESPs, with a nominal free resonance frequency of 75kHz and a spring constant of 2.8N/m. The tip radius is specified to be 20nm, and the front and back are coated with a 10nm/150nm layer of Co/Cr giving a conductive path from the electronics down to the tip apex for electrical experiments.

4.2.1 Vertical Piezoresponse Force Microscopy

To probe the ferroelectric polarization of our samples, we have used a technique derived from contact mode AFM: vertical piezoresponse force microscopy (PFM) [17]. With the tip in contact the sample back electrode is grounded and an oscillating voltage is applied to the tip. Due to the converse piezoelectric effect (the application of a voltage giving rise to a mechanical deformation) the sample surface will start oscillating at the same frequency as the tip excitation. However, due to the material being ferroelectric, this oscillation will either be in phase or out of phase with the original signal, depending on the polarization orientation at the position of the tip. In order to detect this phase we use a lock-in amplifier with the vertical deflection as the input. Since the AFM feedback loop is not fast enough, the oscillation will not be compensated by the motion of the Z column and can be used in order to extract the piezoresponse. A related technique, lateral PFM, consists in the monitoring of the horizontal deflection, providing a piezoresponse in plane to an out-of-plane excitation [12]. An example of vertical PFM measurement is presented in Fig. 4.7, with the phase difference of 180° indicading two opposite out-of-plane domain orientations, and the amplitude dropping to zero at the location of the domain wall. The PFM measurements presented here have, unless otherwise noted, been taken by exciting the tip electrically with the Nanonis OC4 phase locked loop

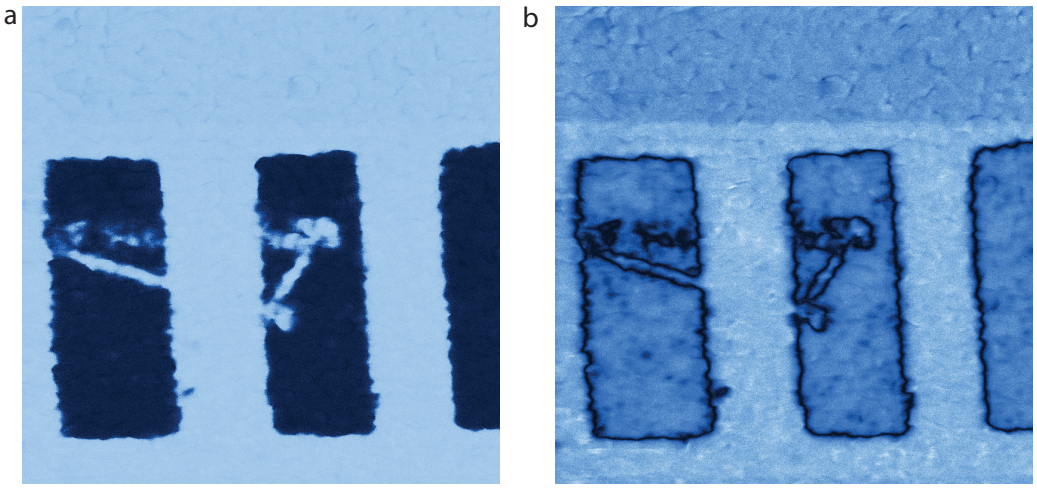

Figure 4.7: Vertical PFM image of poled stripe domains on a PZT sample. (a) Phase, showing clear 180° contrast between the two opposite polarization orientations. (b) Amplitude, showing a drop to zero at the location of the domain wall.

controller at a frequency of 1kHz to the tip, with an AC electric excitation amplitude of 1V. The OC4 and a Stanford Research SR830 lock-in was used to acquire the phase and amplitude of the piezoresponse.

4.2.2 Conductive Atomic Force Microscopy

In order to measure the current going through the system with conductive-AFM, the microscope is configured into contact mode or tapping mode and the tip is brought in contact with the sample. Then, while the microscope feedback loop regulates the Z position, a current preamplifier connected either to the tip or the back electrode converts the current passing through the sample to the system ground to a voltage, which is fed into data acquisition electronics. A typical configuration inspired by the scanning tunneling microscopy world would have the preamplifier connected on the tip with a possibility to apply a voltage to the sample in order to bias the system. Conductive-AFM is a useful technique allowing us to probe the electronic characteristics of the samples at the nanoscale in order to extract conductivity, resistivity and current-voltage characteristics. However, due to the small size of the tip apex and of the tip metal coating, a good ohmic contact with the sample cannot be consistently maintained because of the easier wear of the metallic coating, and thus the effects of tip degradation are most prominent in this AFM mode.

The preamplifier used in this research is an Omicron VT PRE E preamplifier, used for STM measurements, with a dual gain of $1 \cdot 10^{-9} A/V$ and $1 \cdot 10^{-10} A/V$. It was connected directly to the tip and contained the electronics allowing us to bias the tip in series with the current reading, removing the need for a sample bias. This allowed for measurements with heating and cooling of the sample without having to resort to heavy system modification.

An experiment is a question which Science poses to Nature, and a measurement is the recording of Nature's answer.

Max Planck

5 Domain Wall conduction

In this section we present the results of our work on domain wall conduction in $Pb(Zr_{0.2}Ti_{0.8})O_3$. Due to the monodomain as grown state of our sample, all of the measurements require artificial domain wall creation by electrical poling. This poling is performed by applying a voltage to an AFM tip while scanning it on our 70nm PZT thin film with the SRO back electrode electrically grounded.

First, a checkerboard structure with squares was poled on an as-grown region of the sample. The written structure was first imaged with PFM and the resulting topography, PFM phase and PFM amplitude are shown in Fig. 5.1a-c. Then, conductive-AFM was performed in the same area at a low negative DC tip bias. The resulting current signal is shown in Fig. 5.1d, with the domain wall region being conducting, and the rest of the image remaining insulating within the experimental resolution of our current preamplifier. The vertical average signal profiles of the red region in Fig. 5.1d and the green region in Fig. 5.1e are superposed in Fig. 5.1e with the PFM amplitude signal reversed and normalized to the maximum value of the current. The effective domain wall width as measured by PFM corresponds well with the width of the current signal. This fits qualitatively to the best resolution one can obtain by using a metal coated 45nm radius tip, such as the one used in this experiment. More interestingly, the current signal does not follow any features of the surface topography in an obvious way. Thus, we can clearly attribute the current to the domain wall.

5.1 Conductive or displacive current?

Although the domain wall current signal is visible in conductive-AFM, a scanning tip does not tell us much about the nature of the current. The first question that arises is whether this current is static and due to the domain wall conduction, or if it has a transient origin such as domain nucleation or domain wall motion, since both can contribute to a **displacement** current:

$$I = \frac{\Delta Q}{\Delta t} = I_{cond} + I_{disp} = nq + \frac{\Delta D}{\Delta t} = nq + \frac{\Delta P}{\Delta t}$$

which shows that a current I, a change of charge Q with time t can either be conductive (I_{cond}) and arise from charge carrier motion nq, or be displacive (I_{disp}) and arise from the reversal in polarization P of the material, which results in a change of the displacement field D.

Polarization reversal, be it through domain nucleation, domain wall creep, or microscopic ir-

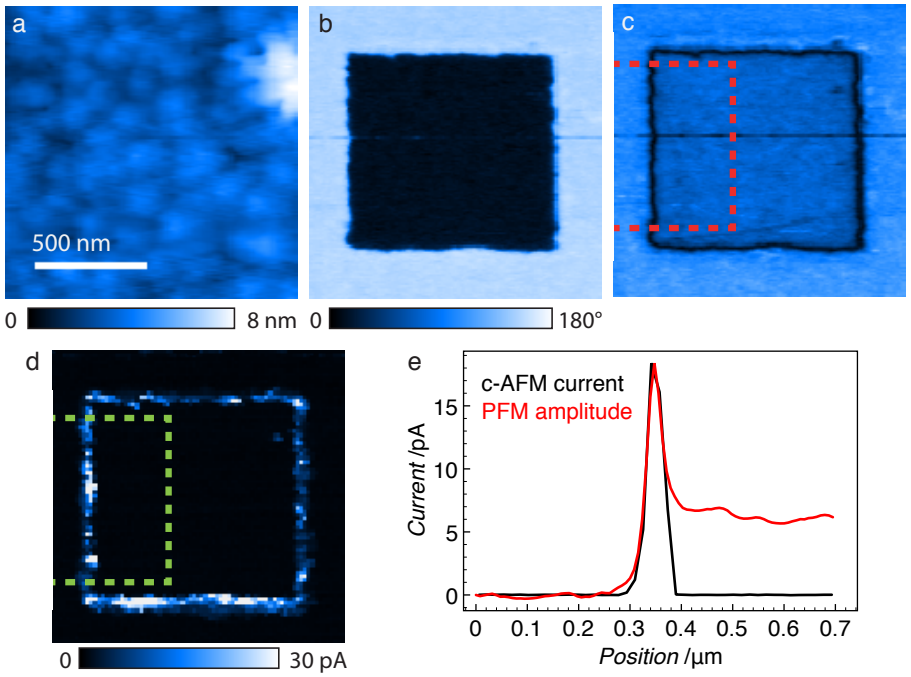

Figure 5.1: Demonstration of domain wall conduction in PZT acquired by atomic force microscopy. The topography (a) was acquired at the same time as the PFM phase (b) and PFM amplitude (c) for a poled domain structure. The conductive-AFM image in (d) was acquired separately with a -1.5V bias. The line profiles of the inverted and normalized PFM amplitude and conductive-AFM are plotted in (e), showing the lateral extent of the domain wall.

reversible changes in domain wall structure at a scale smaller or comparable to the domain wall thickness will not contribute to the current after it is complete and will manifest itself as a current accompanied by changes in the domain structure, with an eventual a decay in current as the domain wall region extends beyond the tip contact. A true conductive current will however persist until the voltage is removed and not be associated with any change in the domain configuration. Thus, the best way to discriminate between the two sources using an AFM is to position the tip just above a domain wall and measure the current while a voltage is applied during a given period of time carefully comparing the PFM image before and after the current acquisition. For this, a domain structure was poled and imaged with PFM (Fig. 5.2a). The tip was then positioned at several locations inside of the domain and at the domain walls. A constant voltage of 1.0V and 1.5V was applied for a duration of 120s and the current was recorded during the application of the voltage, shown in Fig. 5.2c-f. A subsequent PFM image (Fig. 5.2b) was used to compare the domain structure and determine whether domain wall motion, and thus polarization switching, occured. A reference current measurement at -1.0V tip bias was first taken in the interior of the domain (white circle of Fig. 5.2a), far from any domain walls. It is shown in Fig. 5.2c, and was used to calibrate the preamplifier for zero current for the current-voltage measurements. Several measurements were performed at the domain wall, and most of the time there were no changes in domain structure before and after, as shown in PFM (green circles in Fig. 5.2a-b). In these cases the current was found to have a constant 0.5pA level at -1.0V, such as the one shown in Fig. 5.2d, and did not decay during the 120s of measurement. In some cases, for the same 1.0V applied at the AFM tip, however, a sharp current spike feature was observed, 2-3 orders of magnitude higher than the small, stable 0.5pA current (Fig. 5.2e), accompanied by a distinct modification of the domain structure, as shown by the red circles. At -1.5V, all of the measurements in the series showed a current spike right at the beginning, with a tail decaying to zero, once again accompanied by bubble-like protrusions of the polarized domain. From this measurement, we can conclude that two regimes exist: the current is displacement dominated at higher voltages, and conduction

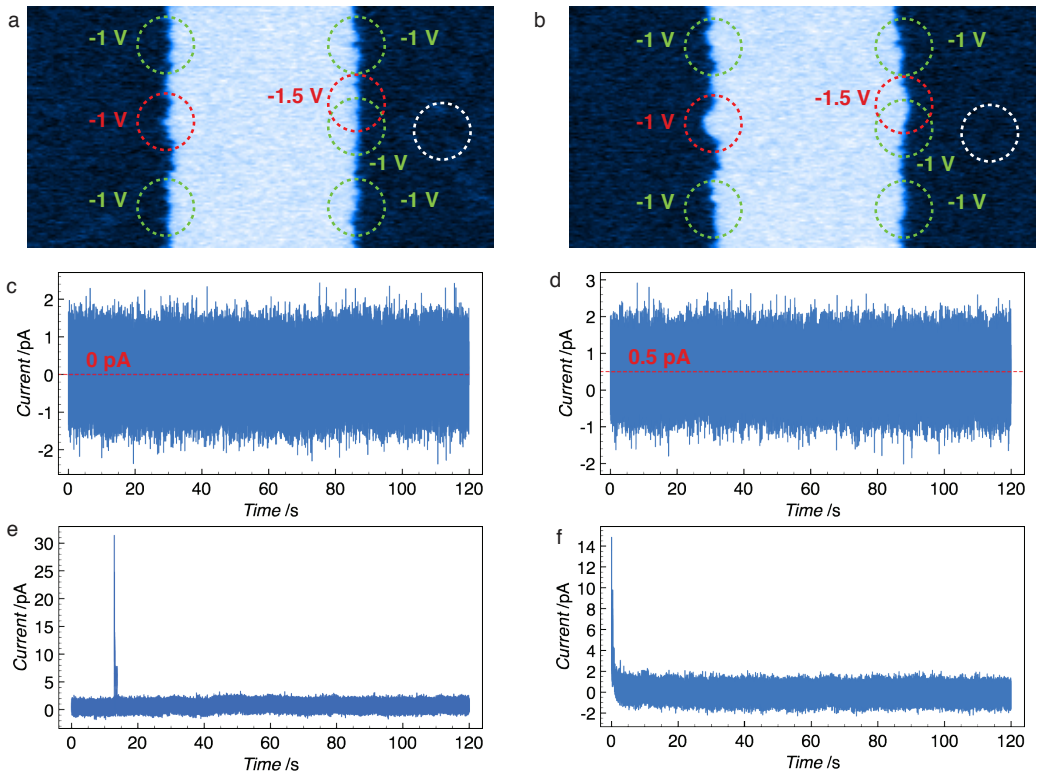

Figure 5.2: Position and hold measurements on a poled domain structure. The 2μm wide PFM images were taken before (a) and after (b) the measurements. The reference measurement (c) was taken at the center of the domain (in the white circle) in order to calibrate the zero level of the current preamplifier. The measurements in green circles show a persistent current level such as the one in (d) at -1.0V tip bias, with no visible changes in domain structure in the subsequent PFM. Measurements with domain structure changes show sharp current spikes either partway such as in (e) at -1.0V tip bias, or initially such as in (f) followed by a decrease and stabilization at -1.5V tip bias.

dominated at lower voltages. In between, we infer the presence of a "crossover region". [1]

Having established the existence of both a conductive and a displacive regime present at domain walls, measurements at different DC tip voltages were taken in order to better understand the current-voltage relationship. This was done by measuring alternating PFM and conductive-AFM scans at increasing voltages in order to track both the current and any changes in domain structure. A subset of these measurements is shown in Fig. 5.3a for negative DC voltages, with the first column being the PFM preceeding the adjacent column's conductive-AFM image. The voltages used for current measurements are indicated in red on the conductive-AFM images. The process was carried out at increasing DC voltages until complete polarization switching occured. The measurement were then repeated on another section of the domain structure for positive DC voltages (Fig. 5.3), until complete switching of the area occured. Averages over the vertical slow scan axis of the conductive-AFM images were calculated and an average current for each voltage was extracted, as shown in Fig. 5.3c for negative and in Fig. 5.3d for positive tip voltages, respectively. The current was found to increase with the magnitude of applied voltage, with a strong asymmetry between positive and negative voltage. For positive voltages, the currents were lower for higher voltage magnitudes. Above a critical threshold (-1.625V

[1] A numerical integration of charge over the displacive measurement in Fig. 5.2e ($6.5 \cdot 10^{-11}$C) and over the conductive measurement in Fig. 5.2d ($3.5 \cdot 10^{-11}$C) yields switched areas of 121μm^2 and 64μm^2 respectively with a polarization value of 50$\mu C/cm^2$. This is an absurd quantity compared to less than 50nm incursions observed for the switched regions.

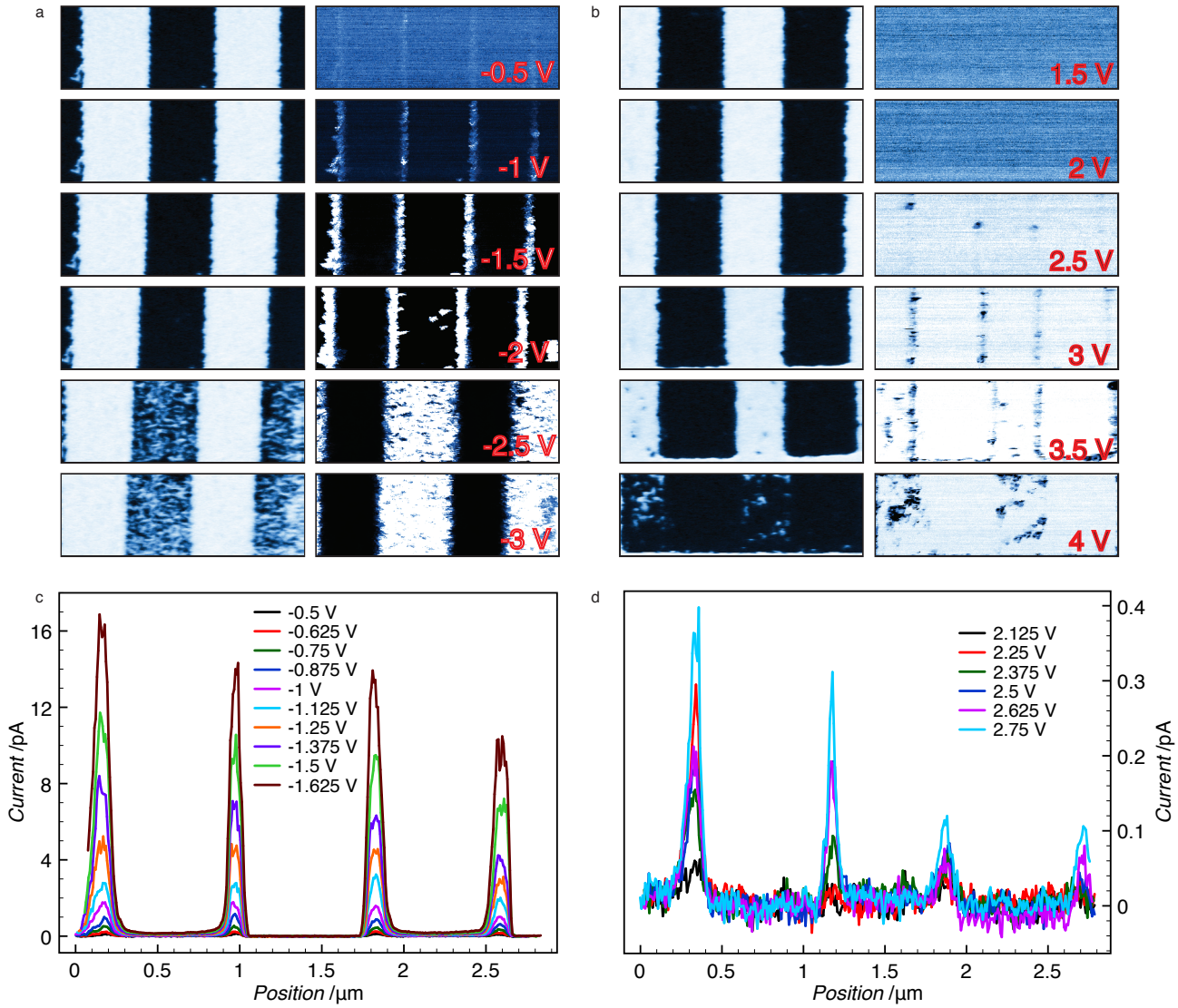

Figure 5.3: Alternating PFM and conductive-AFM images of a poled domain structure measured at increasing negative (a) and positive (b) voltages to the tip until complete reversal of polarization occurred. The averages over the vertical slow scan direction are presented for measurement up to domain structure change for negative (c) and positive (d) voltages.

for negative and 2.75V for positive), changes in the domain structure inseparable from the domain wall signal occurred and the current was measured to be orders of magnitude higher than before in these areas. Due to the nature of conductive-AFM measurements, the duration of voltage application at any given point in space is much shorter than for position-and-hold measurements presented above. Thus, we measure up to voltages well above the ones where current spikes were observed, indicating a possible reversal of domain wall motion.

Two of the four domain walls measured in Fig. 5.3 were selected for the computation of the current-voltage relationship, an shown in Fig. 5.4a. The voltage threshold for the calculation was given by the lowest voltage at which domain structure changes inseparable from the domain wall signal were observed, and was given by -2.125V for negative and 3.25V for positive voltages. This is illustrated with the contrast between Fig. 5.4b-c, a measurement performed at -1.625V with no obvious changes in domain structure, and Fig. 5.4d-e, measured at -2.25V, where orders of magnitude higher current appears at the interior of the domain and at the domain walls, with the subsequent PFM presenting clear changes. At this point, we clearly show, for the full voltage range: a primarily conductive current at the lower extremes and a strongly displacive current at the upper extreme of the range. In between, the gradual current increase

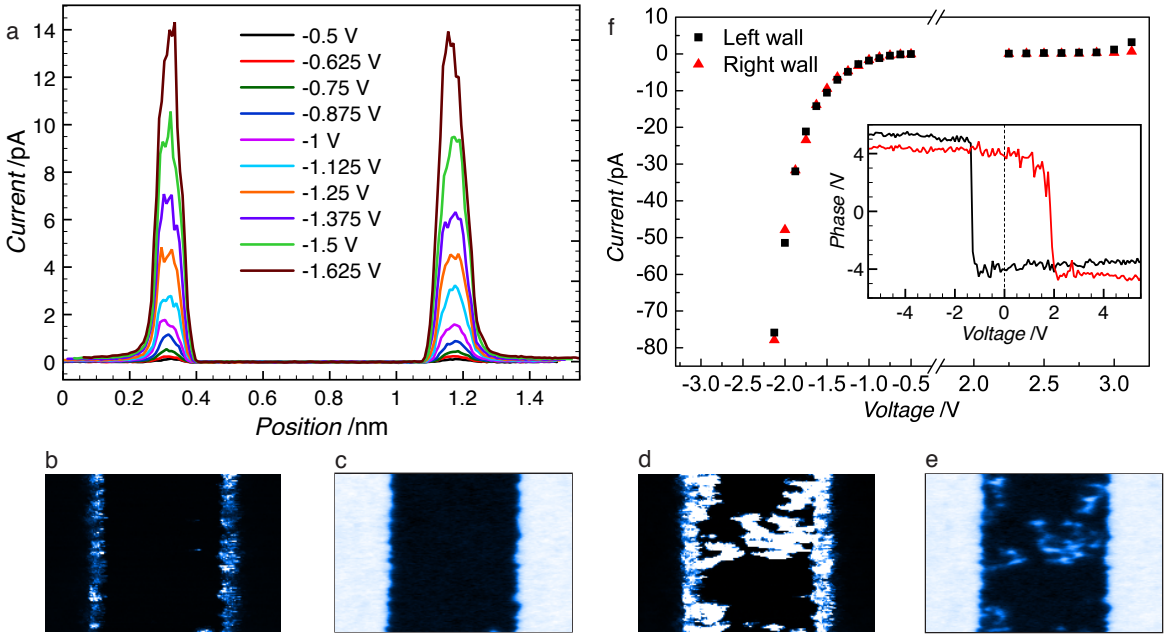

Figure 5.4: (a) The conductive-AFM signal was averaged over the vertical slow scan axis for different values of negative voltages for two domain walls. (b) Conductive-AFM signal at -1.625V, with (c) its subsequent PFM measurement. (d) Conductive-AFM signal at -2.25V showing high current in the domain bulk, confirmed by subsequent PFM in (e). (f) The highly asymmetric average domain wall current voltage relationship extracted from PFM/conductive-AFM series with the polarization versus voltage measurement in inset.

implies a crossover, with possibly some microscopic **reversible** domain wall motion in the electric field [18, 34]. An indication of this was seen during the acquisition of the current at the same time as a PFM image, with a 2.0V AC tip bias (Fig. 5.5). The domain wall current signal (Fig. 5.5c) is of the order of 100pA and is due to switching of very small regions of the domain structure. The current versus voltage relationship was extracted from both walls by taking the

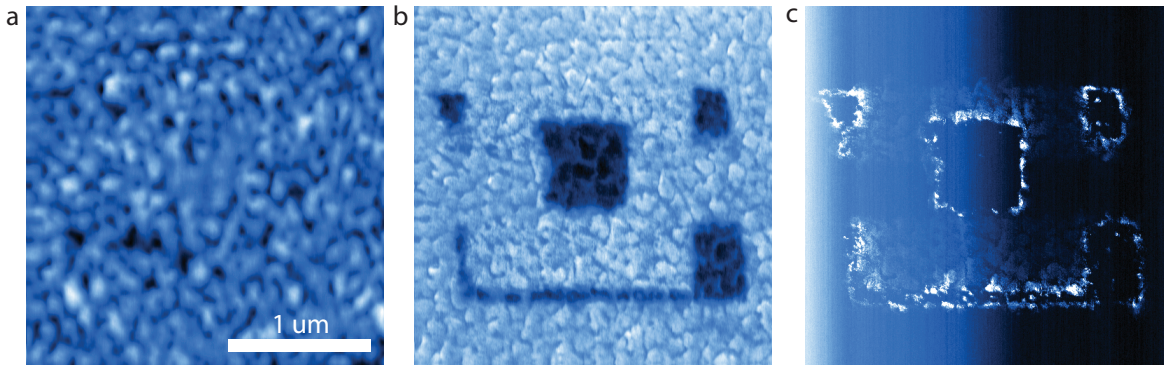

Figure 5.5: AC conductive-AFM image of a poled *smiley* structure: (a) AFM topography, (b) PFM phase and (c) current acquired simultaneously, with no application of DC voltage at an AC bias of 2.0V at 20kHz. The domain wall signal is clearly visible and shows levels of the order of 100pA, indicating switching of small portions of the domain structure. The gradient in the current signal background is due to the frequency response of the preamplifier electronics, primarily designed for DC measurements.

maximum values of the average current. The resulting curve is shown in Fig. 5.4f, with red and black dots representing the right and left domain walls respectively. The most striking feature of this curve is its asymmetry, first with the current threshold (-0.5V for negative and 2.25V

for positive voltages), and second with the difference of magnitude of the positive and negative currents. This is similar to the asymmetry observed for polarization switching. The inset of Fig. 5.4f shows a polarization versus voltage hysteresis loop, performed by sweeping a DC tip voltage simultaneously with the AC component for the PFM measurement and thus acquiring the phase and amplitude of the sample piezoresponse as a function of the applied DC voltage, allowing us to extract the coercive voltages for the polarization switching in both orientations. These are found to be asymmetric, due to the sample boundary conditions. Indeed, the sample has different electrodes on the surface (AFM tip) and at the back of the thin film (SRO) creating different Schottky barriers, which in turn create an in-built electric field throughout the sample.

Combining the position-and-hold measurements with the conductive-AFM/PFM series, we conclusively deduce the existence of several conduction regimes. At low voltages, conductive currents dominate. At high voltages, strongly displacive currents take place. The intermediate values of voltage, where a current increase is observed, are a crossover region with possibly microscopic changes in the domain position, or reversible domain wall motion.

5.2 Temperature dependence

To better understand the current-voltage dependence, we also explored thermal effects on domain wall conduction. Several of the conduction mechanisms applying to the ferroelectrics described in Chapter 3 involve non-trivial temperature dependence. Thus, measurements of the current-voltage characteristic curves at different temperatures are essential in order to discriminate between the dominant conduction mechanism. These measurements were performed using liquid nitrogen at four different temperatures: 120K, 150K, 290K and 330K. A domain structure, shown in Fig. 5.6a was first written at room temperature. For each of the cryogenic measurements, an area of this structure (red regions of Fig. 5.6a) was imaged as follows. A grid of 16x16nm pixels was defined using the AFM software, and the tip was successively positioned at each of the grid points, and a ramp measurement was performed by sweeping the voltage between zero and a negative voltage V_{max}. After the whole grid was finished, it was repeated with a higher magnitude of V_{max}. The measurements taken in this way were averaged over the domain wall length and over the different voltages in order to yield a single current-voltage characteristic curve per temperature, as shown in Fig. 5.6b. The method for the averaging is described in Appendix B. The measurements indicate that there is a clear thermal dependence of the domain wall current for the measurements at 290K and 330K, whereas there is no thermal effects for 120K and 150K. The conduction threshold voltage, defined for these measurements as the voltage at which the current is 1pA is shown in the inset of Fig. 5.6b. For the measurements at 120K and 150K the threshold voltage is equal and drops for 290K and 330K, showing that the conduction mechanism is thermally activated for higher temperatures, with a decrease in conduction threshold and increase in current magnitude.

5.3 Static versus dynamic

Although we demonstrated above that there were no changes in domain structure between before and after the conductive-AFM measurements, it was not possible to probe the nanoscale domain wall structure simultaneously. Thus, hysteresis measurements had a vital role in understanding the nature of the conduction mechanism. A domain structure was poled at room temperature, and grid spectroscopy measurements were performed as described above, with the acquisition of the forward and backward current during each voltage sweep at each range $0 \rightarrow V_{max}$. The hysteresis map for each voltage was then calculated from the data by using:

$$H(V) = \int (I_{fwd}(V) - I_{bwd}(V))dV$$

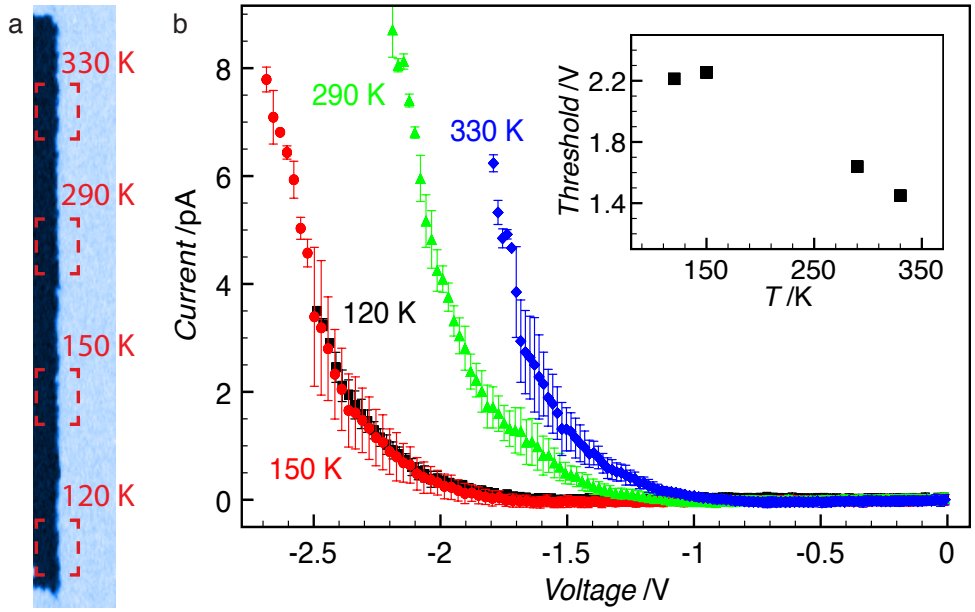

Figure 5.6: Thermal dependence of the average current-voltage characteristic curve. A poled structure (a) is used for grid spectroscopy measurements at different temperatures. The average current-voltage curves for each temperature are then plotted in (b), showing a thermal activation for 290K and 330K. The conduction threshold voltage at which the current is above 1pA is plotted in the inset shows a decrease in threshold for the measurements at 290K and 330K.

with H the integral over the sweep range yielding the hysteresis at a given position and I_{fwd}/I_{bwd} the current during the forward/backward voltage sweep. The method for the extraction of these local hysteresis maps from our measurements is described in Appendix C. Moreover, in order to compare our results with the work of Maksymovych *et al*, we have also calculated a global hysteresis for each voltage, by extracting an average current-voltage curve for each grid spectroscopy measurement, as described in Appendix A. From these local and global hysteresis data, four distinct regimes were observed:

- - **-0.9V<voltage**: Neither conduction nor hysteresis are detected at these voltages for both the local and the global hysteresis. We are below the conduction threshold for these series of measurements and the current is below the noise level of the preamplifier.
- - **-1.4V<voltage<-0.9V**: A domain wall current is visible, such as in Fig. 5.7a, but the calculation of the local hysteresis map does not yield a visible hysteresis, as shown in Fig. 5.7b. The global hysteresis does not show any opening. We are thus probably in the conduction regime, with no changes to the domain structure and no domain wall motion.
- - **-2.7V<voltage<-1.5V**: At these voltages, there is a strong current still localized at the domain walls like in Fig. 5.7c, with a bidirectional local hysteresis (Fig. 5.7d) appearing at the location of the domain wall. There is no global hysteresis present, suggesting very small (microscopic) evolution of the domain walls, (ir-)reversibly adapting to their potential landscape under the influence of the field.
- - **voltage<-2.8V**: In this voltage range, the current signal (Fig. 5.7e) is orders of magnitude higher and is also present inside of the domain with the local hysteresis map in Fig. 5.7f showing a unidirectional switching. The global hysteresis shows an opening (red curve in Fig. 5.7g). This looks like a clearly displacive current associated with large scale domain wall motion and polarization switching, also inside the domains.

When put together, these measurements demonstrate:

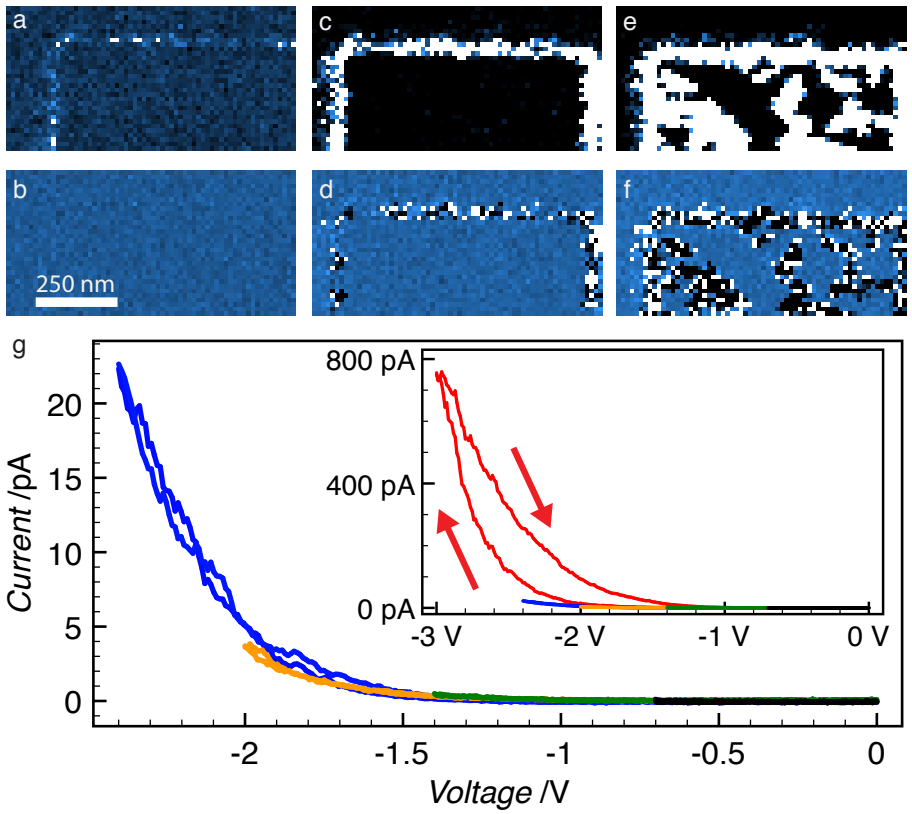

Figure 5.7: The hysteretic behavior of the domain wall current voltage characteristic curves is shown in this figure. (a),(c) and (e) are c-AFM images taken at sweep ranges up to -1.4V, -2.0V and -3.0V respectively. The corresponding calculated local hysteresis maps ($\int I_{fwd} - I_{bwd}$) are shown in (b),(d) and (f) respectively. Three regimes are visible, with no hysteresis at all in (b), a small bidirectional hysteresis local to the domain wall (d) and a large hysteresis in the bulk of the domain (f). The global hysteresis can be seen from the difference between the forward and backward current-voltage curves in (g). There is no hysteresis until the switching voltage (red line in the inset) is reached, in contrast with the local hysteresis maps.

1. Two regimes are present: conductive at low voltages and displacive at high voltages. There is a crossover region in-between.

2. The conductive current is **stable** over measurement durations of 120s.

3. Clear thermal activation at **higher temperatures**, and an apparent *freezing in* for lower temperatures.

Begin thus from the first act, and proceed; and, in conclusion, at the ill which thou hast done, be troubled, and rejoice for the good.

Pythagoras

6 Conduction mechanism

In this section, we apply the electrical conduction mechanisms presented in Chapter 3 to the current voltage characteristic curves extracted from the measurements performed on domain walls.

6.1 AFM tip field modeling

Experimentally, only the voltage applied to the tip is known. In the case of parallel plate capacitors in vacuum separated by a distance d, the field dependence on voltage is trivial:

$$E = V/d$$

However, inside the real device configuration, with the possibility of a complex dielectric response, and the potential effects of interfacial dead layers and other defects, the exact electric field in the material is generally unknown, which poses a problem for most of the conduction mechanisms considered. Moreover, in the case of a ferroelectric, the polarization will render the relationship even more complex. Thus, in order to understand the microscopic origin of the conduction, one first has to understand the relationship between the voltage and the electric field.

Although the exact defect configurations are unknown and obviously not possible to take into account, the general behavior can be modeled with increasing accuracy depending on initial assumptions. We use a relatively simple model, taking the manufacturer-specified parameters for the tip apex radius (20nm) and opening angles (20°), with the tip held at the experimentally applied bias boltage V, impose rotational symmetry around the axis passing through the center of the tip, and model the PZT as a 70nm dielectric layer with a metallic back electrode held at ground potential. The modeling was done with *COMSOL Multiphysics v3.5*, a finite element analysis and solver software. A geometry of the model (Fig. 6.1) was prepared and then divided into a fine mesh with increasing resolution at the interfaces, and the system was iteratively solved numerically for the relevant differential equations at each node until a stationary solution was found. Two cases were considered during modeling. The first assumed that the dielectric constant of the ferroelectric is a constant, with $\varepsilon = 100$, in agreement with experimentally obtained values for PZT [50]. The second was to postulate that due to imperfect screening, charge accumulation in a small layer (skin depth) below the surface will enhance the dielectric constant. For this, the expression of the dielectric constant was set to decay within a

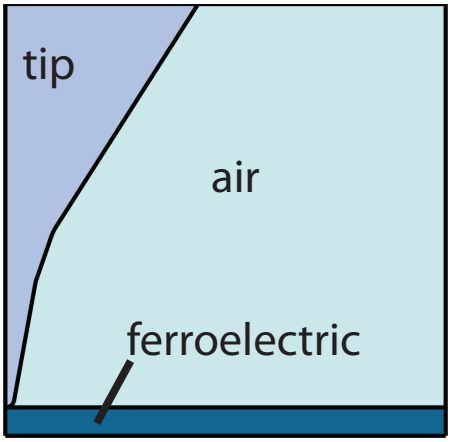

Figure 6.1: Geometry used for modeling the electric field in the ferroelectric material due to an AFM tip in contact. The tip radius is 20nm and the opening angle is 20°, becoming 40° after 500nm. The ferroelectric is represented by a 70nm thick dielectric film with $\varepsilon = 100$ and the system bathes in air.

nanometer scale to its bulk value in the depth of the film (z in nanometers):

$$\varepsilon(z) = 100 + \frac{1000}{\pi}\left(\frac{0.1}{((z \cdot 10^9)^2 + (0.1)^2)}\right)$$

The resulting electric field distributions are shown in Fig. 6.2a for the uniform ε, and in Fig. 6.2b for the case of a skin charge layer. Taking a cross-section along the thickness of the sample just below the tip apex, one can extract the electric field profiles as shown in Fig. 6.2c with the solid black line for the uniform ε and solid red line for the skin layer case. The dielectric constants are shown with dashed lines and corresponding colors and guidelines with z^{-1} and z^{-2} dependencies are presented for the electric field.

Since there was no dramatic difference between the two cases, $\varepsilon = 100$ was retained for its simplicity for further modeling. The model was then tested against different voltages and the resulting electric field distributions are shown in Fig. 6.3.

An important result of this simple model is that, although the electric field is highly inhomogeneous, both radially and within the depth of the film, it does show a linear dependence on voltage, as demonstrated by the inset of Fig. 6.3, which shows a linear relationship between the field maxima and the voltage. Thus, although this model does not take the work functions or the physical properties of the materials into account, it shows that $E \propto V$ in this simple case, justifying the use of this substitution in the analysis to follow.

6.2 Current-voltage analysis

In order to understand the domain wall conduction mechanism, the current-voltage characteristic curves extracted from the grid spectroscopy measurements for different temperatures were represented in linearized coordinates corresponding to the different expressions of the current-voltage dependence for the conduction mechanisms presented earlier. From these representations, we could extract the relevant physical quantities (optical dielectric constant, exponents in power law behavior and possible thermal dependence), and compare these to known or expected values for PZT or similar ferroelectric thin films, and thus judge the applicability of a given conduction mechanism.

For SCL, a linearization of $I \propto V^n$ is shown in Fig. 6.4a, and shows very high values of

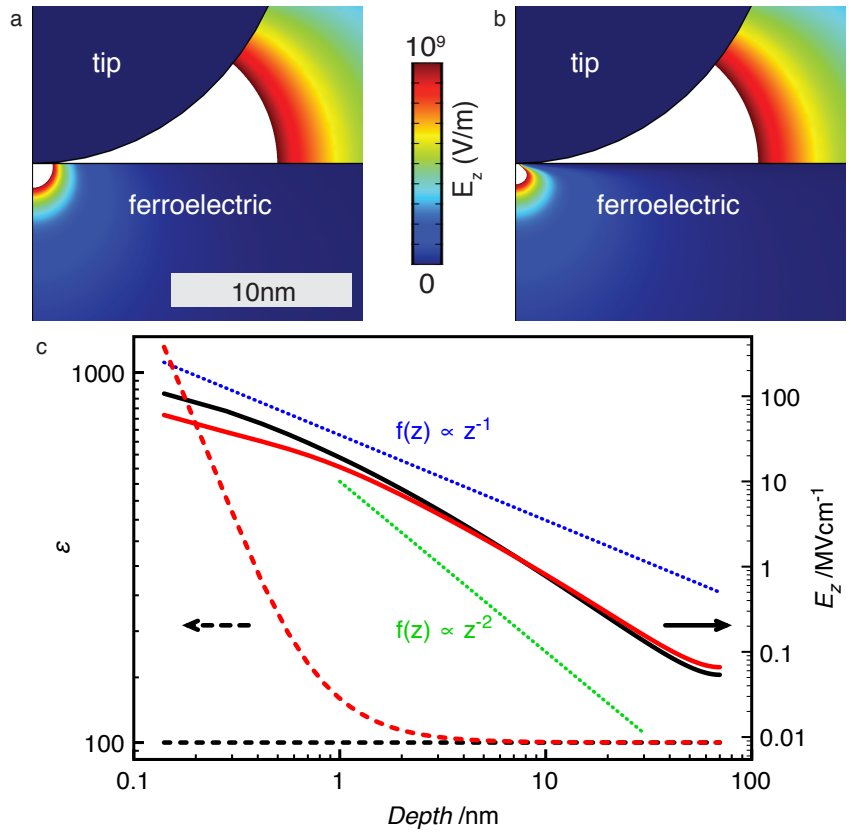

Figure 6.2: Model for the electric field generated by a biased AFM tip into a ferroelectric thin film. (a) Out of plane component of the electric field into the film with a uniform dielectric constant. (b) Out of plane component of the electric field into the film with a skin layer due to an increased screening at the tip-ferroelectric interface. (c) The electric field (right axis) and dielectric constant (left axis) under the tip as a function of the depth into the film for the two scenarios for the dielectric constants. Guidelines for a z^{-1} and z^{-2} dependence are shown for the electric field.

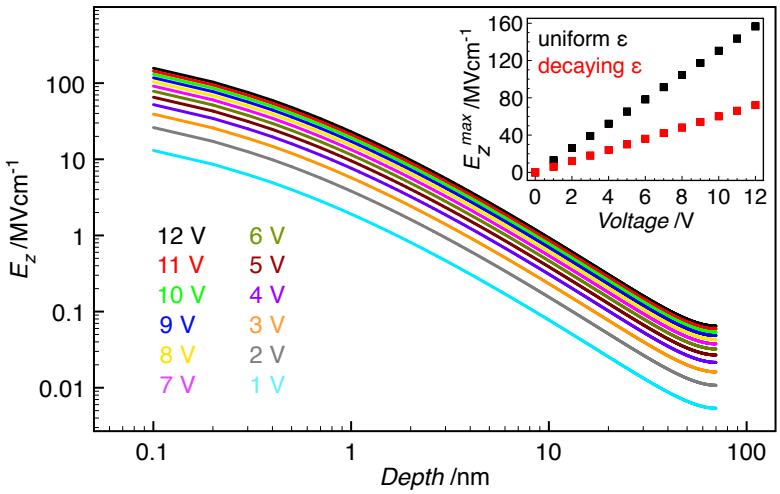

Figure 6.3: The electric field distribution below the surface of the ferroelectric as a function of tip bias. The electric field maxima are plotted in the inset.

the exponent n. Thus, the continuous trap distribution limit ($n = 2$) is not a possible scenario. The alternative for SCL conduction would be a discrete trap distribution within the band gap, but in this case the power law growth exponent n should show a temperature dependence $n-1$ $= T_1/T$. As shown in the inset, for $n-1$ versus $1/T$, no such dependence can be extracted.

Thus, we can conclude that SCL conduction is not a likely candidate for the microscopic mechanism describing the domain wall conduction.

The representation of the current versus voltage data for the normalized coordinates of FN, SE and PF/RSS (the latter two mechanisms present the same formal current-voltage relationship for the linearization) shows very good linearization in Fig. 6.4b-d for all three cases. This is essentially to be expected, as we are performing log-log fits on relatively small data sets. Thus, to discriminate between the different mechanisms and find which best fits the experimental situation, we need to consider also the role of the temperature (although being careful, since we only have 4 data points, and already know that the temperature dependence itself is complex), and whether the physical characteristics extracted from the linearized fits to the different mechanisms give anything realistic and valid. We note here that, as shown in the model above, the electric fields near the region of contact between the tip and the ferroelectric thin film are extremely high. Combined with the asymmetry of the current-voltage characteristic with the dominating contribution for the negative voltages to the tip in which the Schottky barriers between the film and the electrode appear to play a significant role, this strongly suggests an interface-limited tunneling or emission-type mechanism where the rate-limiting step is the passage of charge carriers of these barriers, either classically or via quantum processes.

However, Fowler-Nordheim, the only tunneling mechanism, can be immediately eliminated, because the slopes in its linearization with $log(I/V^2) \propto 1/V$ show a strong thermal variation. However, this slope, $\frac{8\pi\sqrt{2m^*}}{3qh}$, should be completely temperature-independent.

In the emission-type mechanisms, where charges from the tip can classically overcome the Schottky barriers under thermal activation, we considered the possibility of both standard Schottky thermionic emission (although it is less likely because of the low mobilities in ferroelectrics), and the adapted Richardson-Schottky-Simmons equation. Schottky thermionic emission yields a good fit with a $log(I) \propto V^{1/2}$ linearization (Fig. 6.4c). We can calculate the dielectric constant by extracting it from the linearized slope $\beta = \frac{e}{k_B T}\left(\frac{e}{4\pi\varepsilon\varepsilon_0}\right)^{1/2}$. The expected value for ε should be given by the lower bound of the optical dielectric constant $\varepsilon_\infty = 6$, since if one supposes that the carrier mobility is not too low, they will only spend a short time near the potential barrier maximum [52]. However, the calculated values of ε remove SE from the list of possible mechanisms due to their unphysical values (it is not physical to have a permittivity lower than for vacuum).

We have then considered RSS as a possible mechanism, which was physically more favorable than SE due to the low mobility and short mean free path for ferroelectrics. The linearized coordinates are identical for PF and RSS, with a factor 4 difference in the final extracted value for the dielectric constant, $\varepsilon_{PF} = 4\varepsilon_{RSS}$, with the key difference being the exact form of the temperature dependence. A good linearization in term of $log(I/V) \propto V^{1/2}$ was obtained (Fig. 6.4d), and the calculated dielectric constants for the different temperatures are show in the inset. The values obtained are more realistic than for SE but still lower than expected for PZT [52].

From this part of the analysis we can conclude that the conduction mechanism is RSS or PF, and given the actual device configuration, with the dominant role of the interfaces and very high fields, the likely scenario is an interface limited mechanism, RSS. Moreover, the bulk mobility contained in the expression for RSS suggests that this mechanism is more than *purely* interfacial. We also note that in high k dielectric oxides, a hybrid mechanism was proposed: tunneling or emission aided PF [24]. A more detailed study of the temperature dependence of the conduction is required in order to discriminate between all of the possible conduction mech-

anisms. For tunneling aided PF, for instance, the activation energies would correspond to the Schottky barrier heights, rather than the activation energy distribution expected in the normal PF mechanism. Another possible way to discriminate between RSS and PF, an interface limited and a bulk limited mechanism, is a study of conduction as a function of film thickness. If the conduction mechanism is interface limited, we would not expect any changes with thickness.

The analysis would not be complete without a verification for the case when the field does

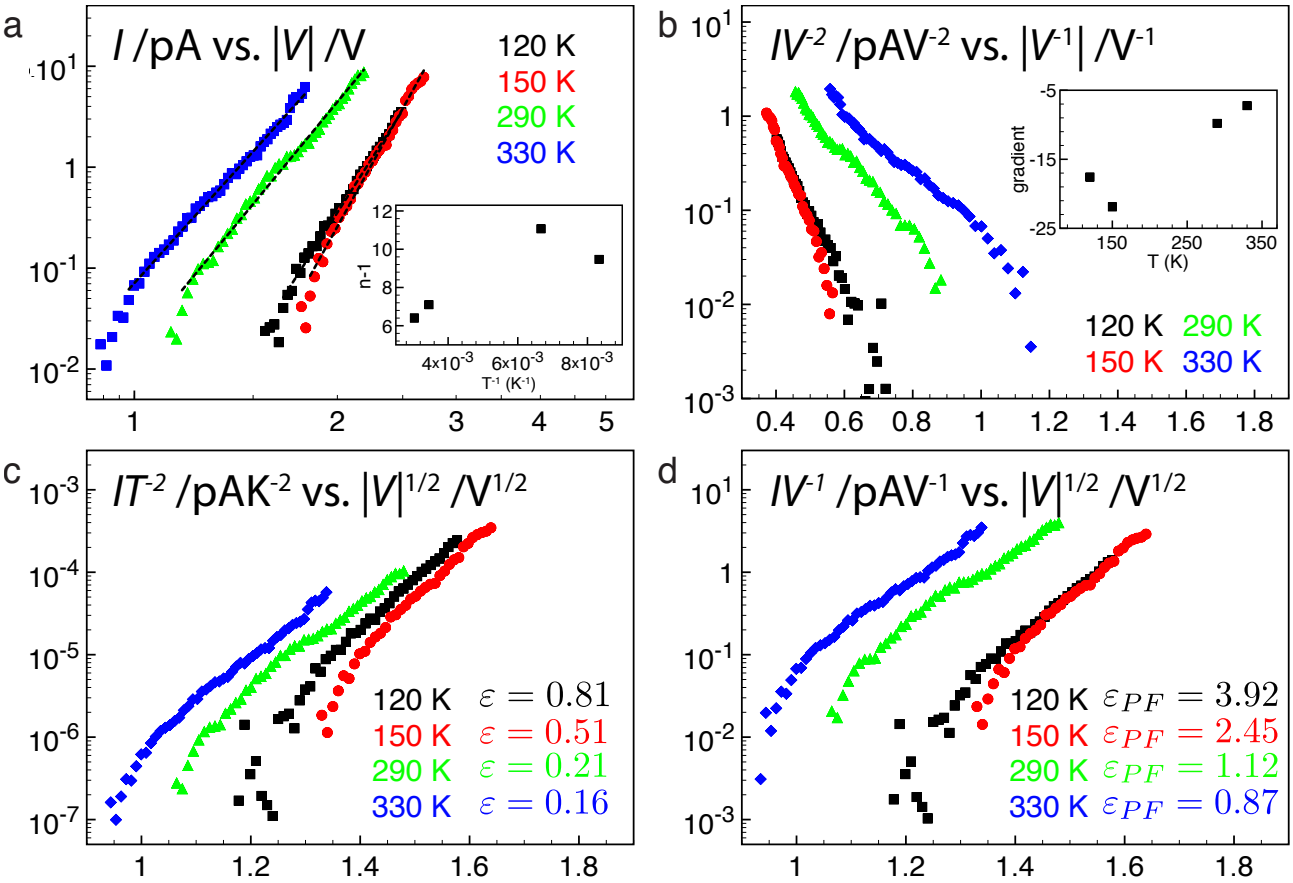

Figure 6.4: Analysis of the current-voltage characteristic curves as a function of temperature in light of the aforementioned conduction mechanisms. (a) Space charge limited conduction mechanism, with $\log(I) \propto n \log(V)$. The inset shows the temperature dependence $n - 1 \propto 1/T$. (b) Fowler Nordheim conduction mechanism linearization, with $\log(I/V^2) \propto 1/V$, with the gradient in function of the temperature in the inset. (c) Schottky thermionic emission linearization with $\log(I/T^2) \propto V^{1/2}$, with the extracted dielectric constants in the inset. (d) Poole-Frenkel or Richardson-Schottky-Simmons mechanisms linearizations, with $\log(I/V) \propto V^{1/2}$. The Poole-Frenkel dielectric constants are shown in the inset with $\varepsilon_{PF} = 4\varepsilon_{RSS}$.

not follow the $E \propto V$ dependency, but instead is of the form of the partial depletion, or abrupt junction, such as described for the Schottky thermionic emission mechanism, with $E = \sqrt{\frac{2qN_D}{\varepsilon_{dc}\varepsilon_0}\left(V + V_{bi} - \frac{k_B T}{q}\right)}$ [37]. This can apply to our system because for the case of a ferroelectric capacitor, charge screening the polarization near the surface changes the maximum field in that region and makes the reverse-bias Schottky barrier at the interface with the electrode the limiting factor for electric transport. Once represented in normalized coordinates taking into account the built-in voltage, the current-voltage relationship shows a reasonable linearization to the SE or FN mechanisms. In order to extract the optimal value of the built-in bias V_{bi}, a systematic test for fit quality with a range of values between -1.5V and 1.5V was performed for each temperature by iterative fitting and parameter adjustement. The method for this fit is presented in Appendix D. The values for the best fits for the FN mechanism are given

in Fig. 6.5b, and are found to be very low. Moreover, just as for the $E \propto V$ case the gradients of the linearization (28, 32, 18 and 15 for 120, 150, 290 and 330K respectively) are shown to strongly vary with temperature, although from the FN mechanism they should be temperature independent. For SE, Fig. 6.5a gives the best fit values of V_{bi}, as well as the calculated dopant density N_D with the standard dielectric constant values $\varepsilon_{DC} = 400$ and $\varepsilon_\infty = 6$. These range between $3.09 \cdot 10^{26}$ and $3.76 \cdot 10^{28}$, which are both unphysically high, especially for the highest temperatures. Nevertheless, a linearization for the built-in voltage of 1.0V is shown in Fig. 6.5d.

a

T (K)	V_{bi} (V)	N_D (m^{-3})
120	1.12	3.09×10^{26}
150	1.2	1.11×10^{27}
290	0.82	5.49×10^{27}
330	0.24	3.76×10^{28}

b

T (K)	V_{bi} (V)
120	0.19
150	-0.01
290	0.02
330	-1.2

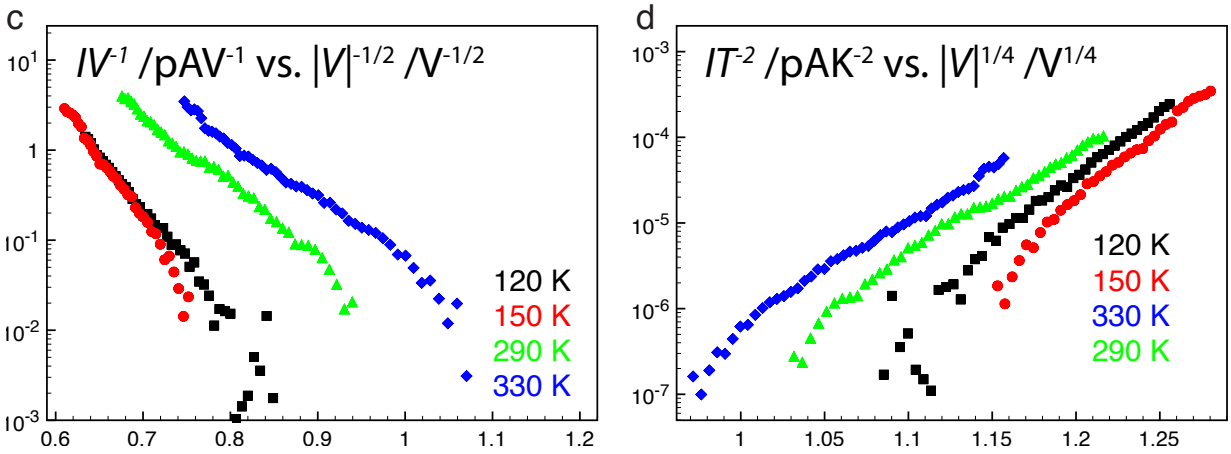

Figure 6.5: The best values of the fits for built-in voltage V_{bi} and the dopant densities are shown in (a) for the Schottky thermionic emission mechanism, for the different temperatures. In (b), the built-in voltage V_{bi} values are extracted from the best fits for the Fowler-Nordheim mechanism. The Fowler-Nordheim (c) and Schottky thermionic emission (d) linearizations in normalized coordinates for values of V_{bi} of 0.0V and 1.0V respectively.

6.3 Microscopic origin of conduction

To better understand the conduction mechanism, we also need to consider the microscopic origins of the conduction. The main question to address is why is only the wall conducting not the bulk, such as in tunneling electroresistance measurements where a Fowler-Nordheim conduction of the samples was modulated by the polarization orientation [19, 21, 9, 31]. The results and analysis presented above point to a thermally activated domain-wall conduction. Moreover, the Schottky diode-like asymmetric current versus voltage relationship shows that the trap states near the interface between the ferroelectric and the electrodes play a crucial role.

At the microscopic level, TEM measurements of our samples (in Chapter 4) show a very small amount of a-axis inclusions, the granular structure related to the growth mode of the films - more island-like than step-flow growth - and also carry through the defect structures present in the STO substrates. Like other ferroelectric films, we also believe that our samples present oxygen vacancies. All such defects can have a significant influence of the configuration of the

domain wall and the stability of the domain structure. Previous studies [36, 35] have shown that in similar PZT thin films, domain wall pinning in the disorder potential provided by the defects, which competes with the elastic properties of the wall, governs both the static and dynamic behavior. Spectroscopic switching PFM (SSPFM) studies [42] showed the variation of this disorder potential locally on the surface and the actual pinning effects of an individual oxygen vacancy defect [41, 25]. DFT calculations [23] show that the energy of an oxygen vacancy and domain wall complex is lower than that of the individual components separately - suggesting that with sufficient defect mobility, these would segregate preferentially at the domain walls, and provide a possible pathway for conduction. In BFO thin films, it has in fact been shown that oxygen vacancy densities strongly influence domain wall conduction [44]. We believe that a similar effect can be expected in PZT.

We are thus likely to have a higher concentration of defects, potentially charge carriers, and also states for electrons in the ferroelectric band gap, all at the domain wall. Taken together, we can suggest that in thicker films, outside of the tunneling limits, the bulk is not conductive enough. However, once the charge gets past the Schottky barrier, there may be enough charge carriers and trap states present at the domain wall for the electrons so that conduction can locally proceed.

A partial support for such a scenario comes from the recent high resolution TEM measurements of 180° domain walls in PZT carried out by Jia *et al* [27]. These clearly show segments of charged domain walls, which would need to be screened if they are to be thermodynamically stable. The necessary screening could well be provided by charged defects, further increasing the local charge carrier density at the domain wall, and making it locally more conductive than the bulk o the domain.

7
Conclusion and outlook

In conclusion, we have clearly demonstrated domain wall conduction in a ferroelectric tetragonal material, PZT. We have demonstrated the stable behavior of the current signal, and have found that fits from the measured current-voltage characteristics for the conduction mechanisms of PF/RSS provided the best fits and physical parameters. We have also discussed the role of defects at the domain wall as the microscopic origin of the observed conduction. The described scenario of defect segregation at charged domain walls is not unique to PZT, and can in fact be present in most ferroic materials, with strain and boundary conditions playing a key role in the potential device applications.

Since this work was published [22], research in the field of domain wall conduction has continued to yield new results. Wu *et al* have reported the discovery of domain wall conduction in $HoMnO_3$, a hexagonal ferroelectric, which possesses a nontrivial domain wall configuration [51]. For instance, it is a unique material in the sense that the domain walls are known to be charged, providing a testbed for the theories on conductivity in charged walls. Du *et al* have announced domain wall conduction in oxygen deficient $YMnO_3$ [10], where they have invoked the ordering of oxygen vacancies at domain walls as the main source of this phenomenon. In the same tone, Farokhipoor and Noheda [14] detail the local conductivity and role of oxygen vacancies in twin walls in BFO, proposing that the vacancies migrate to the location of the domain wall.

Keeping in mind the results we have obtained so far, we would like to pursue the following in the continuation of the experiments:

- A study of domain wall conduction as a function of temperature, since the very few points of data we have gathered in the current study do not allow us to comfortably discuss the thermal dependence of the observed conduction.

- A study of domain wall conduction as a function of sample thickness, which will help discriminate between bulk or interface conduction mechanism.

- A study of domain wall conduction as a function of boundary conditions, which will help understand better the mechanisms behind the metal-ferroelectric interfaces. This includes the deposition of nano-electrodes and fabrication of devices such as described in [45] as well as growth of PZT on different substrate/back electrode combinations.

- From a more fundamental point of view, a study of single crystal versus thin film behavior, with the combination of PFM, conductive-AFM and TEM studies of the influence of the intrinsic domain wall structure on the observed conduction.

8 Bibliography

References

[1] *MultiMode SPM Instruction Manual v4.31ce.* Digital Instruments.

[2] A. Aird and E. K. H. Salje. Sheet superconductivity in twin walls: experimental evidence of WO_{3-x}. *Journal of Physics: Condensed Matter*, 10(22):L377, 1998.

[3] D. I. Bilc, R. Orlando, R. Shaltaf, G.-M. Rignanese, J. Íñiguez, and Ph. Ghosez. Hybrid exchange-correlation functional for accurate prediction of the electronic and structural properties of ferroelectric oxides. *Phys. Rev. B*, 77:165107, Apr 2008.

[4] G. Binnig, C. F. Quate, and Ch. Gerber. Atomic force microscope. *Phys. Rev. Lett.*, 56:930–933, Mar 1986.

[5] G. Catalan, H. Béa, S. Fusil, M. Bibes, P. Paruch, A. Barthélémy, and J. F. Scott. Fractal dimension and size scaling of domains in thin films of multiferroic $BiFeO_3$. *Phys. Rev. Lett.*, 100:027602, Jan 2008.

[6] G. Catalan and J. F. Scott. Physics and applications of bismuth ferrite. *Advanced Materials*, 21(24):2463–2485, 2009.

[7] G. Catalan, J. Seidel, R. Ramesh, and J. F. Scott. Domain wall nanoelectronics. *Rev. Mod. Phys.*, 84:119–156, Feb 2012.

[8] Y.-P. Chiu, Y.-T. Chen, B.-C. Huang, M.-C. Shih, J.-C. Yang, Q. He, C.-W. Liang, J. Seidel, Y.-C. Chen, R. Ramesh, and Y.-H. Chu. Atomic-scale evolution of local electronic structure across multiferroic domain walls. *Advanced Materials*, 23(13):1530–1534, 2011.

[9] A. Crassous, V. Garcia, K. Bouzehouane, S. Fusil, A. H. G. Vlooswijk, G. Rispens, B. Noheda, M. Bibes, and A. Barthelemy. Giant tunnel electroresistance with $PbTiO_3$ ferroelectric tunnel barriers. *Applied Physics Letters*, 96(4):042901, 2010.

[10] Y. Du, X. L. Wang, D. P. Chen, S. X. Dou, Z. X. Cheng, M. Higgins, G. Wallace, and J. Y. Wang. Domain wall conductivity in oxygen deficient multiferroic $YMnO_3$ single crystals. *Applied Physics Letters*, 99(25):252107, 2011.

[11] E. A. Eliseev, A. N. Morozovska, G. S. Svechnikov, V. Gopalan, and V. Ya. Shur. Static conductivity of charged domain walls in uniaxial ferroelectric semiconductors. *Phys. Rev. B*, 83:235313, Jun 2011.

[12] L. M. Eng, H.-J. Guntherodt, G. Rosenman, A. Skliar, M. Oron, M. Katz, and D. Eger. Nondestructive imaging and characterization of ferroelectric domains in periodically poled crystals. *Journal of Applied Physics*, 83(11):5973–5977, 1998.

[13] S. Farokhipoor and B. Noheda. Conduction through 71° domain walls in $BiFeO_3$ thin films. *Phys. Rev. Lett.*, 107:127601, Sep 2011.

[14] S. Farokhipoor and B. Noheda. Local conductivity and the role of vacancies around twin walls of (001)-$BiFeO_3$ thin films. *arXiv:1201.0144*, Dec 2011.

[15] D. D. Fong, G. B. Stephenson, S. K. Streiffer, J. A. Eastman, O. Auciello, P. H. Fuoss, and C. Thompson. Ferroelectricity in ultrathin perovskite films. *Science*, 304(5677):1650–1653, 2004.

[16] R. H. Fowler and L. Nordheim. Electron emission in intense electric fields. *Proceedings of the Royal Society of London. Series A*, 119(781):173–181, 1928.

[17] K. Franke, J. Besold, W. Haessler, and C. Seegebarth. Modification and detection of domains on ferroelectric PZT films by scanning force microscopy. *Surface Science*, 302(1-2):L283 – L288, 1994.

[18] P. Gao, C. T. Nelson, J. R. Jokisaari, S.-H. Baek, C. W. Bark, Y. Zhang, E. Wang, D. G. Schlom, C.-B. Eom, and X. Pan. Revealing the role of defects in ferroelectric switching with atomic resolution. *Nature Communications*, 2, DEC 2011.

[19] V. Garcia, S. Fusil, K. Bouzehouane, S. Enouz-Vedrenne, N. D. Mathur, A. Barthelemy, and M. Bibes. Giant tunnel electroresistance for non-destructive readout of ferroelectric states. *Nature*, 460(7251):81–84, JUL 2 2009.

[20] S. Gariglio, N. Stucki, J.-M. Triscone, and G. Triscone. Strain relaxation and critical temperature in epitaxial ferroelectric $Pb(Zr_{0.2}Ti_{0.8})O_3$ thin films. *Applied Physics Letters*, 90(20):202905, 2007.

[21] A. Gruverman, D. Wu, H. Lu, Y. Wang, H. W. Jang, C. M. Folkman, M. Ye. Zhuravlev, D. Felker, M. Rzchowski, C.-B. Eom, and E. Y. Tsymbal. Tunneling electroresistance effect in ferroelectric tunnel junctions at the nanoscale. *Nano Letters*, 9(10):3539–3543, 2009.

[22] J. Guyonnet, I. Gaponenko, S. Gariglio, and P. Paruch. Conduction at domain walls in insulating $Pb(Zr_{0.2}Ti_{0.8})O_3$ thin films. *Advanced Materials*, 23(45):5377–5382, 2011.

[23] L. He and D. Vanderbilt. First-principles study of oxygen-vacancy pinning of domain walls in $PbTiO_3$. *Phys. Rev. B*, 68:134103, Oct 2003.

[24] D. S. Jeong and C. S. Hwang. Tunneling-assisted poole-frenkel conduction mechanism in HfO_2 thin films. *Journal of Applied Physics*, 98(11):113701, 2005.

[25] S Jesse, B. J. Rodriguez, S. Choudhury, A. P. Baddorf, I. Vrejoiu, D. Hesse, M. Alexe, E. A. Eliseev, A. N. Morozovska, J. Zhang, L.-Q. Chen, and S. V. Kalinin. Direct imaging of the spatial and energy distribution of nucleation centres in ferroelectric materials. *Nature Materials*, 7(3):209–215, MAR 2008.

[26] C.-L. Jia, S.-B. Mi, K. Urban, I. Vrejoiu, M. Alexe, and D. Hesse. Atomic-scale study of electric dipoles near charged and uncharged domain walls in ferroelectric films. *Nature Materials*, 7(1):57–61, JAN 2008.

[27] C.-L. Jia, K. W. Urban, M. Alexe, D. Hesse, and I. Vrejoiu. Direct observation of continuous electric dipole rotation in flux-closure domains in ferroelectric $Pb(Zr,Ti)O_3$. *Science*, 331(6023):1420–1423, 2011.

[28] C. Kittel. Theory of the structure of ferromagnetic domains in films and small particles. *Phys. Rev.*, 70:965–971, Dec 1946.

[29] D. Lee, R. K. Behera, P. Wu, H. Xu, Y. L. Li, S. B. Sinnott, S. R. Phillpot, L. Q. Chen, and V. Gopalan. Mixed bloch-néel-ising character of 180° ferroelectric domain walls. *Phys. Rev. B*, 80:060102, Aug 2009.

[30] C. Lichtensteiger, J.-M. Triscone, J. Junquera, and P. Ghosez. Ferroelectricity and tetragonality in ultrathin $PbTiO_3$ films. *Phys. Rev. Lett.*, 94:047603, Feb 2005.

[31] P. Maksymovych, S. Jesse, P. Yu, R. Ramesh, A. P. Baddorf, and S. V. Kalinin. Polarization control of electron tunneling into ferroelectric surfaces. *Science*, 324(5933):1421–1425, 2009.

[32] P. Maksymovych, J. Seidel, Y. H. Chu, P. Wu, A. P. Baddorf, L.-Q. Chen, S. V. Kalinin, and R. Ramesh. Dynamic conductivity of ferroelectric domain walls in $BiFeO_3$. *Nano Letters*, 11(5):1906–1912, 2011.

[33] B. Meyer and D. Vanderbilt. *Ab initio* study of ferroelectric domain walls in $PbTiO_3$. *Phys. Rev. B*, 65:104111, Mar 2002.

[34] C. T. Nelson, P. Gao, J. R. Jokisaari, C. Heikes, C. Adamo, A. Melville, S.-H. Baek, C. M. Folkman, B. Winchester, Y. Gu, Y. Liu, K. Zhang, E. Wang, J. Li, L.-Q. Chen, C.-B. Eom, D. G. Schlom, and X. Pan. Domain dynamics during ferroelectric switching. *Science*, 334(6058):968–971, 2011.

[35] P. Paruch, T. Giamarchi, and J.-M. Triscone. Domain wall roughness in epitaxial ferroelectric $Pb(Zr_{0.2}Ti_{0.8})O_3$ thin films. *Phys. Rev. Lett.*, 94:197601, May 2005.

[36] P. Paruch, T. Giamarchi, T. Tybell, and J.-M. Triscone. Nanoscale studies of domain wall motion in epitaxial ferroelectric thin films. *Journal of Applied Physics*, 100(5):051608, 2006.

[37] L. Pintilie and M. Alexe. Metal-ferroelectric-metal heterostructures with schottky contacts. i. influence of the ferroelectric properties. *Journal of Applied Physics*, 98(12):124103, 2005.

[38] S. Poykko and D. J. Chadi. Ab initio study of 180° domain wall energy and structure in $PbTiO_3$. *Applied Physics Letters*, 75(18):2830–2832, 1999.

[39] S. Pöykkö and D. J. Chadi. Dipolar defect model for fatigue in ferroelectric perovskites. *Phys. Rev. Lett.*, 83:1231–1234, Aug 1999.

[40] N. M. Ravindra and J. Zhao. Fowler-nordheim tunneling in thin SiO_2 films. *Smart Materials and Structures*, 1(3):197, 1992.

[41] B. J. Rodriguez, Y. H. Chu, R. Ramesh, and S. V. Kalinin. Ferroelectric domain wall pinning at a bicrystal grain boundary in bismuth ferrite. *Applied Physics Letters*, 93(14):142901, 2008.

[42] B. J. Rodriguez, S. Jesse, M. Alexe, and S. V. Kalinin. Spatially resolved mapping of polarization switching behavior in nanoscale ferroelectrics. *Advanced Materials*, 20(1):109–114, 2008.

[43] J. F. Scott and M. Dawber. Oxygen-vacancy ordering as a fatigue mechanism in perovskite ferroelectrics. *Applied Physics Letters*, 76(25):3801–3803, 2000.

[44] J. Seidel, P. Maksymovych, Y. Batra, A. Katan, S.-Y. Yang, Q. He, A. P. Baddorf, S. V. Kalinin, C.-H. Yang, J.-C. Yang, Y.-H. Chu, E. K. H. Salje, H. Wormeester, M. Salmeron, and R. Ramesh. Domain wall conductivity in la-doped $BiFeO_3$. *Phys. Rev. Lett.*, 105:197603, Nov 2010.

[45] J. Seidel, L. W. Martin, Q. He, Q. Zhan, Y. H. Chu, A. Rother, M. E. Hawkridge, P. Maksymovych, P. Yu, M. Gajek, N. Balke, S. V. Kalinin, S. Gemming, F. Wang, G. Catalan, J. F. Scott, N. A. Spaldin, J. Orenstein, and R. Ramesh. Conduction at domain walls in oxide multiferroics. *Nature Materials*, 8(3):229–234, 2009.

[46] J. G. Simmons. Richardson-schottky effect in solids. *Phys. Rev. Lett.*, 15:967–968, Dec 1965.

[47] S. K. Streiffer, J. A. Eastman, D. D. Fong, C. Thompson, A. Munkholm, M. V. Ramana Murty, O. Auciello, G. R. Bai, and G. B. Stephenson. Observation of nanoscale 180° stripe domains in ferroelectric $PbTiO_3$ thin films. *Phys. Rev. Lett.*, 89:067601, Jul 2002.

[48] S. M. Sze and K. K. Ng. *Physics of semiconductor devices*. John Wiley & Sons, Inc., Berlin, 2006.

[49] E. Y. Tsymbal and H. Kohlstedt. Tunneling across a ferroelectric. *Science*, 313(5784):181–183, 2006.

[50] I. Vrejoiu, G. Le Rhun, L. Pintilie, D. Hesse, M. Alexe, and U. Gosele. Intrinsic ferroelectric properties of strained tetragonal PbZr0.2Ti0.8O3 obtained on layer-by-layer grown, defect-free single-crystalline films. *Advanced Materials*, 18(13):1657–1661, 2006.

[51] W. Wu, Y. Horibe, N. Lee, S.-W. Cheong, and J. R. Guest. Conduction of topologically protected charged ferroelectric domain walls. *Phys. Rev. Lett.*, 108:077203, Feb 2012.

[52] P. Zubko, D. J. Jung, and J. F. Scott. Electrical characterization of $PbZr_{0.4}Ti_{0.6}O_3$ capacitors. *Journal of Applied Physics*, 100(11):114113, 2006.

A

Current-voltage extraction

The program below calculates an average current-voltage relationship for the grid spectroscopy images for the domain wall. It takes the average over the three spectroscopy sections centered at the position of the wall along the whole length of the domain wall, returning a single current-voltage curve corrected for the preamplifier linear noise contribution.

```
import os
import string
import shroomy
from numpy import *
import matplotlib.pyplot as plt
import tkFileDialog

def run(program, *args):
    # find executable
    for path in string.split(os.environ["PATH"], os.pathsep):
        file = os.path.join(path, program) + ".exe"
        try:
            return os.spawnv(os.P_DETACH, file, (file,) + args)
        except os.error:
            pass
    raise os.error, "cannot find executable"

shroomy.DEBUG_ENABLE = False

# IMPORT FILES AND PARAMS

# select working directory
currdir = tkFileDialog.askdirectory()
os.chdir(currdir)
# open working directory
#run('explorer',os.getcwd())
# get cutoff values (to separate domain walls)
cutoff = genfromtxt('cutoffs.txt')
# check if grid has to be chopchopped
dochop = 0
if os.path.exists('chopchop.txt'):
    chop = genfromtxt('chopchop.txt')
    dochop = 1
# change directory to spectro files
```

```
os.chdir(currdir + '\\spectro\\')
# import spectro files
files = os.listdir('.')
files_spectro = [f for f in files if f.endswith('.3ds')]

# CALCULATE MEAN I-V CURVE FOR EACH FILE

plt.figure()

for curr_file in files_spectro:
    curr = shroomy.export_vmax_slice(curr_file)
    if dochop == 1:
        curr = curr[:,int(chop[0]):int(chop[1])]
    # get start and end bias from header
    hdr = shroomy.read_header_at_position(0,0)
    print('Extracting average I-V curve at V = {0}\nFile = {1}\n'.format(hdr[1],
        curr_file))
    # fit I-V on nonconducting region to estimate preamp noise contribution
    xval = linspace(hdr[0],hdr[1],shroomy.grid_points)
    noise_fwd = shroomy.read_data_at_position(0,0,0)
    noise_bwd = shroomy.read_data_at_position(0,0,1)
    noise_fit_fwd = polyfit(xval, noise_fwd, 1)
    noise_fit_bwd = polyfit(xval, noise_bwd, 1)
    # matrices for fwd and bwd I-V curves on current maxima
    iv_fwd = zeros((len(cutoff)-1,shroomy.grid_points))
    iv_bwd = zeros((len(cutoff)-1,shroomy.grid_points))

    for k in range(len(cutoff)-1):
        # find the position of current max for each column
        cutmin = int(cutoff[k])
        cutmax = int(cutoff[k+1])
        curr_tmp = curr[cutmin:cutmax,:]
        currmax = curr_tmp.max(0)
        currmaxpos = curr_tmp.argmax(0)

        # sum averages over 3 pixels of the I-V curves at max I
        for i in range(len(currmaxpos)):
            y = currmaxpos[i]
            if y == 0:
                tmp = (matrix(shroomy.read_data_at_position(i,y+1+cutmin,0))+
                    matrix(shroomy.read_data_at_position(i,y+cutmin,0))*2)
                iv_fwd[k,:] = iv_fwd[k,:] + tmp/3
                tmp = (matrix(shroomy.read_data_at_position(i,y+1+cutmin,1))+
                    matrix(shroomy.read_data_at_position(i,y+cutmin,1))*2)
                iv_bwd[k,:] = iv_bwd[k,:] + tmp/3
            elif y == cutmax - cutmin-1:
                tmp = (matrix(shroomy.read_data_at_position(i,y-1+cutmin,0))+
                    matrix(shroomy.read_data_at_position(i,y+cutmin,0))*2)
                iv_fwd[k,:] = iv_fwd[k,:] + tmp/3
                tmp = (matrix(shroomy.read_data_at_position(i,y-1+cutmin,1))+
                    matrix(shroomy.read_data_at_position(i,y+cutmin,1))*2)
                iv_bwd[k,:] = iv_bwd[k,:] + tmp/3
            else:
                tmp = (matrix(shroomy.read_data_at_position(i,y-1+cutmin,0))+
                    matrix(shroomy.read_data_at_position(i,y+cutmin,0))+matrix(
                    shroomy.read_data_at_position(i,y+1+cutmin,0)))
                iv_fwd[k,:] = iv_fwd[k,:] + tmp/3
                tmp = (matrix(shroomy.read_data_at_position(i,y-1+cutmin,1))+
                    matrix(shroomy.read_data_at_position(i,y+cutmin,1))+matrix(
                    shroomy.read_data_at_position(i,y+1+cutmin,1)))
                iv_bwd[k,:] = iv_bwd[k,:] + tmp/3
        # divide to get I-V curve averaged over whole wall
        iv_fwd[k,:] /= len(currmaxpos)
```

```
89          iv_bwd[k,:] /= len(currmaxpos)
            # substract preamp noise
91          iv_fwd[k,:] -= noise_fit_fwd[0]*xval + noise_fit_fwd[1]
            iv_bwd[k,:] -= noise_fit_bwd[0]*xval + noise_fit_bwd[1]
93
            # PLOT
95          plt.plot(xval, iv_fwd[k,:])
            plt.plot(xval, iv_bwd[k,:])
97
            # SAVE
99          savetxt('..\\avg_IV\\' + curr_file.replace('.3ds','') + '_wall_' + str(k
                +1) + '.txt', column_stack([xval, iv_fwd[k,:], iv_bwd[k,:]]))

101 plt.show()
```

B

Full current-voltage characteristic extraction

The program below extracts a full averaged current-voltage characteristic curve from a set of grid spectroscopy measurements, with a statistical error included.

```
import os
import string
import shroomy
from numpy import *
import matplotlib.pyplot as plt
import tkFileDialog

shroomy.DEBUG_ENABLE = False

# IMPORT FILES AND PARAMS

# select working directory
currdir = tkFileDialog.askdirectory()
os.chdir(currdir)
# get cutoff values (to separate domain walls)
cutoff = genfromtxt('cutoffs.txt')
# get number of files before switching
mibs = genfromtxt('maxivbeforeswitching.txt')
# change directory to spectro files
os.chdir(currdir + '\\avg_IV\\')
# import spectro files
allfiles = os.listdir('.')

for k in range(len(cutoff)-1):
    all_iv = matrix([[],[],[]])
    all_iv = all_iv.transpose()
    cntr = 0
    files = [f for f in allfiles if f.endswith(str(k+1)+'.txt')]
    for curr_file in files:
        print('Extracting I-V curve from {0}'.format(curr_file))
        if cntr < int(mibs[k]):
            curr_iv = genfromtxt(curr_file)
            all_iv = vstack((all_iv,curr_iv))
            cntr = cntr+1

    # MAGIC - sorta...
```

```
    all_iv = all_iv[argsort(all_iv[:,0],0),:]
    all_iv = all_iv[:,0,:]

    iv_hist = histogram(all_iv[:,0],bins=100)
    iv_hist_nbins = iv_hist[0]
    iv_hist_labels = iv_hist[1]
    start_index = 0
    x = []
    y_fwd = []
    y_bwd = []
    for i in range(len(iv_hist_nbins)):
        x.append((iv_hist_labels[i+1]+iv_hist_labels[i])/2)
        y_fwd.append(mean(all_iv[start_index:start_index+iv_hist_nbins[i],1]))
        y_bwd.append(mean(all_iv[start_index:start_index+iv_hist_nbins[i],2]))
        start_index = start_index + iv_hist_nbins[i]

    plt.scatter(x,y_fwd,c='blue')
    plt.scatter(x,y_bwd,c='red')

    savetxt('..\\histo_iv_wall_' + str(k+1) + '.txt',column_stack([x, y_fwd,
        y_bwd]))

plt.show()
```

C

Local hysteresis map extraction

The program below extracts the local hysteresis maps from the grid spectroscopy files.

```
import os
import string
import shroomy
import im_resize
from numpy import *
import matplotlib.pyplot as plt
import matplotlib.colors as col
import tkFileDialog

def run(program, *args):
    # find executable
    for path in string.split(os.environ["PATH"], os.pathsep):
        file = os.path.join(path, program) + ".exe"
        try:
            return os.spawnv(os.P_DETACH, file, (file,) + args)
        except os.error:
            pass
    raise os.error, "cannot find executable"

shroomy.DEBUG_ENABLE = False

# DEFINE BLUE SCALE FOR IMAGE
cdict = {'red': ((0.0, 0.0, 0.0),
                 (0.999, 51.0/255.0, 1.0),
                 (1.0, 1.0, 0.0)),
         'green': ((0.0, 0.0, 0.0),
                   (0.999, 153.0/255.0, 1.0),
                   (1.0, 1.0, 0.0)),
         'blue': ((0.0, 0.0, 0.0),
                  (0.999, 255.0/255.0, 1.0),
                  (1.0, 1.0, 0.0))}
my_cmap = col.LinearSegmentedColormap('my_colormap',cdict,256)

# IMPORT FILES AND PARAMS

# select working directory
currdir = tkFileDialog.askdirectory()
```

```
# open img directory in explorer
#run('explorer',os.getcwd() + '\\img\\')
# change directory to spectro files
os.chdir(currdir + '\\spectro\\')
# import spectro files
files = os.listdir('.')
files_spectro = [f for f in files if f.endswith('.3ds')]

# GENERATE IMAGES

for curr_file in files_spectro:
    print('Generating hysteresis image for {0}'.format(curr_file))
    shroomy.grid_open(curr_file)
    shroomy.read_header_param()

    hyst = zeros((shroomy.grid_dim_y,shroomy.grid_dim_x))

    for j in range(shroomy.grid_dim_y):
        for i in range(shroomy.grid_dim_x):
            hyst[j][i] = sum(shroomy.read_data_at_position(i,j,0)) - sum(shroomy
                .read_data_at_position(i,j,1))

    plt.imsave('..\\hyst_img\\' + curr_file.replace('.3ds','_hyst.png'),hyst,
        cmap=my_cmap, vmin=-1e-10, vmax=1e-10)

im_resize.rescale_img('..\\hyst_img', 'png', 5)
```

D

Abrupt junction approximation

For the abrupt junction approximation, $E_m = \sqrt{\frac{2qN_D}{\varepsilon_{dc}\varepsilon_0}\left(V + V_{bi} - \frac{k_BT}{q}\right)}$, the linearizations were performed at a set of different built-in voltages, and the best fit was found by maximizing the linear fit R^2 quality factor. Below is the Python program used for this purpose.

```
import os
from numpy import *
from scipy import stats
import matplotlib.pyplot as plt

lower_V_bi =-1
higher_V_bi = 1.4
V_bi_step = 0.01
V_bi = arange(lower_V_bi, higher_V_bi+V_bi_step,V_bi_step)

allfiles = os.listdir(".")
files = [f for f in allfiles if f.endswith(".txt")]
cutoffs = [38, 31, 46, 45]
i = 0
for k in range(len(files)):
  print(files[k])
  iv = genfromtxt(files[k])
  iv = iv[0:cutoffs[k]]
  lni = log(iv[:,1])
  v = []
  r = []
  r2 = 0
  for vbi in V_bi:
    #print("V_bi = {0}".format(vbi))
    vtot = (abs(iv[:,0] + vbi)) ** 0.25
    slope, intercept, r_value, p_value, std_err = stats.linregress(vtot,lni)
    r_value **= 2
    fit = slope*vtot + intercept
    #print(r_value)
    if r_value > r2:
      r2 = r_value
      best_vbi = vbi
    plt.subplot(420+i)
    plt.scatter(vtot,lni,c="blue")
```

```
35      plt.plot(vtot,fit,c="red")
        v.append(vbi)
37      r.append(r_value)
    print("Best Vbi = {0}, with R2 = {1}".format(best_vbi,r2))
39  plt.subplot(421+i)
    plt.plot(v,r)
41  i += 2
plt.show()
```

E

Python 3ds module

The module below allows to extract data and headers from the *Nanonis* 3ds grid spectroscopy format.

```
import os
import sys
import struct
import binascii
from numpy import *
import matplotlib.pyplot as plt

# global variables
# /!\ one can read these variables' values inside functions, but in order
# to modify them, the global keyword has to be called first
DEBUG_ENABLE = True
headerarr = []
grid_data = []
grid_dim_x = []
grid_dim_y = []
grid_center_x = []
grid_center_y = []
grid_width = []
grid_height = []
grid_angle = []
grid_signal = []
grid_fixed_parameters = []
grid_exp_parameters = []
grid_param_count = []
grid_exp_size = []
grid_points = []
grid_channels = []
grid_delay = []
grid_exp = []
grid_date = []
grid_comment = []


# open 3ds file and split content into header and spectroscopy data
def grid_open(filename):
    fd = open(filename,'rb')
```

```
    data = fd.read()
    fd.close()
    dataarr = data.split(':HEADER_END:\r\n')
    header = dataarr[0]
    global grid_data # this contains the spectroscopy data
    grid_data = dataarr[1]
    global headerarr # this contains the header data
    headerarr = header.split('\n')


# retrieve parameters from header
def read_header_param():

    for headerline in headerarr:
        if headerline.startswith('Grid dim'):
            tmp = headerline.split('" ')
            tmp = tmp[1].split(' x ')
            global grid_dim_x, grid_dim_y
            grid_dim_x = int(tmp[0])
            grid_dim_y = int(tmp[1])
            if DEBUG_ENABLE:
                print('Grid dim X=' + str(grid_dim_x) + ' Y=' + str(grid_dim_y))

        if headerline.startswith('Grid settings'):
            tmp = headerline.split('=')
            tmp = tmp[1].split(';')
            global grid_center_x, grid_center_y, grid_width, grid_height,
                grid_angle
            grid_center_x = float(tmp[0])
            grid_center_y = float(tmp[1])
            grid_width = float(tmp[2])
            grid_height = float(tmp[3])
            grid_angle = float(tmp[4])
            if DEBUG_ENABLE:
                print('Grid center X=' + str(grid_center_x) + ' Y=' + str(
                    grid_center_y))
                print('Grid width=' + str(grid_width) + ' height=' + str(
                    grid_height))
                print('Grid angle=' + str(grid_angle))

        if headerline.startswith('Sweep Signal'):
            tmp = headerline.split('" ')
            global grid_param_count
            grid_signal = tmp[1]
            if DEBUG_ENABLE:
                print('Sweep Signal: ' + grid_signal)

        if headerline.startswith('Fixed parameters'):
            tmp = headerline.split('" ')
            global grid_param_count
            grid_fixed_parameters = tmp[1].split(';')
            if DEBUG_ENABLE:
                print('Fixed parameters: ' + str(grid_fixed_parameters))

        if headerline.startswith('Experiment parameter'):
            tmp = headerline.split('" ')
            global grid_param_count
            grid_exp_parameters = tmp[1].split(';')
            if DEBUG_ENABLE:
                print('Experiment parameters: ' + str(grid_exp_parameters))

        if headerline.startswith('# Parameters (4 byte)'):
            tmp = headerline.split('=')
```

```
            global grid_param_count
            grid_param_count = int(tmp[1])
            if DEBUG_ENABLE:
                print('Grid parameter count=' + str(grid_param_count))

        if headerline.startswith('Experiment size (bytes)'):
            tmp = headerline.split('=')
            global grid_exp_size
            grid_exp_size = int(tmp[1])
            if DEBUG_ENABLE:
                print('Grid experiment size=' + str(grid_exp_size))

        if headerline.startswith('Points'):
            tmp = headerline.split('=')
            global grid_points
            grid_points = int(tmp[1])
            if DEBUG_ENABLE:
                print('Grid points=' + str(grid_points))

        if headerline.startswith('Channels'):
            tmp = headerline.split('"')
            global grid_channels
            grid_channels = tmp[1].split(';')
            if DEBUG_ENABLE:
                print('Channels: ' + str(grid_channels))

        if headerline.startswith('Delay before measuring (s)'):
            tmp = headerline.split('=')
            global grid_delay
            grid_delay = float(tmp[1])
            if DEBUG_ENABLE:
                print('Delay before measuring=' + str(grid_delay))

        if headerline.startswith('Experiment='):
            tmp = headerline.split('"')
            global grid_exp
            grid_exp = tmp[1]
            if DEBUG_ENABLE:
                print('Experiment: ' + str(grid_exp))

        if headerline.startswith('Date'):
            tmp = headerline.split('"')
            global grid_date
            grid_date = tmp[1]
            if DEBUG_ENABLE:
                print('Date: ' + str(grid_date))

        if headerline.startswith('Comment'):
            tmp = headerline.split('"')
            global grid_comment
            if len(headerline) > 15:
                grid_comment = tmp[1]
            else:
                grid_comment = "---NO COMMENT---"
            if DEBUG_ENABLE:
                print('Comment: ' + str(grid_comment))


# retrieve spectroscopy data at (x,y) position with channel number 0,...
def read_data_at_position(x,y,channel):
    hdr_offset = grid_param_count*4
    chan_offset = 4*grid_points*channel
    meas_offset = (hdr_offset+chan_offset)
```

```
160     glob_offset = (hdr_offset+grid_exp_size)*(y*grid_dim_x+x)
        start_bias = struct.unpack('!f', grid_data[0:4])[0]
162     end_bias = struct.unpack('!f', grid_data[4:8])[0]
        data_array = []
164     for i in range(grid_points):
            data_array.append(struct.unpack('!f', grid_data[(glob_offset+meas_offset
                +4*i):(glob_offset+meas_offset+4*(i+1))])[0])
166         if DEBUG_ENABLE:
                print(struct.unpack('!f', grid_data[(glob_offset+meas_offset+4*i):(
                    glob_offset+meas_offset+4*(i+1))])[0])
168     return data_array

170 # retrieve spectroscopy data at (x,y) position with channel number 0,...
    def read_header_at_position(x,y):
172     hdr_offset = grid_param_count*4
        glob_offset = (hdr_offset+grid_exp_size)*(y*grid_dim_x+x)
174     data_array = []
        for i in range(grid_param_count):
176         data_array.append(struct.unpack('!f', grid_data[(glob_offset+4*i):(
                glob_offset+4*(i+1))])[0])
            if DEBUG_ENABLE:
178             print(struct.unpack('!f', grid_data[(glob_offset+4*i):(glob_offset
                    +4*(i+1))])[0])
        return data_array
180
    # export a slice of current values at Vmax
182 def export_vmax_slice(filename):
        grid_open(filename)
184     read_header_param()
        currents = zeros((grid_dim_y,grid_dim_x))
186     for j in range(grid_dim_y):
            for i in range(grid_dim_x):
188             data = read_data_at_position(i,j,0)
                currents[j][i] = data[grid_points-1]
190     return currents
```